Mottram, C.M., et al., 2020, Syncing fault rock clocks: Direct comparison of U-Pb carbonate and K-Ar illite fault dating methods: Geology, v. 48, https://doi.org/10.1130/G47778.1

First direct comparison of U-Pb carbonate and K-Ar illite fault dating methods

Data Repository

1. Full Analytical methods

1.1 K-Ar fault gouge dating

1.1.1 Fault gouge clay separation

Samples were frozen using a shell freezer, then freeze-dried such that they were soft enough to gently crush with mortar/pestle before sieving, without damaging/breaking individual grains. About 300-500 g of freeze-dried sample was transferred to a solderless sieve stack (2 mm, 250 µm, 63 µm, catch pan and lid) and sieved for 5 minutes. The contents of the catch pan (<63 µm fraction) were transferred to a stainless steel milkshake bucket with 250 mL of distilled water. The 63-250 µm fraction was then wet sieved to obtain any additional <63 µm grains still present in that fraction. The <63 µm fraction was mixed in a milkshake bucket using a mixer stand for 2 minutes and then alternately centrifuged, decanted and washed in triplicate for each size fraction. Final clay size fractions were freeze-dried.

1.1.2 K-Ar methodology

Conventional K-Ar dating was selected for this study vs. the encapsulation $^{40}Ar/^{39}Ar$ method, since the latter, especially regarding fine-grained clay minerals, is affected by ^{39}Ar recoil during sample irradiation and requires non-standardized corrections (Clauer et al., 2012).

Detailed accounts of the conventional K-Ar dating technique have been given by Dalrymple & Lanphere (1969), Faure (1986) and Dickin (1995). Briefly, the ages of rocks or minerals can be determined by measuring the amount of the argon isotope, ^{40}Ar, in the rocks or in individual minerals relative to the potassium content. ^{40}Ar is produced by the decay of an isotope of potassium, ^{40}K. Clays generally contain negligible amounts of argon

when they are formed, although small amounts of atmospheric argon may adhere to the samples, which can be corrected for using the atmospheric $^{40}Ar/^{36}Ar$ ratio of 295.5. Thus, by measuring the ratio of ^{40}Ar to ^{40}K, and knowing the decay rate of ^{40}K, it is possible to calculate the time since the rock or mineral formed.

Potassium content was determined by ICP-OES (Agilent Technologies 725 ICP-OES and a CETAC ASX-520 autosampler). Approximately 20 mg of sample was dissolved with HF and HNO_3 (see for example Heinrichs & Herrmann, 1990). Once in solution, the samples were diluted to 10-50 ppm K for the ICP-OES analysis. The pooled error of K determination of all samples and standards is better than 2 %.

Ar isotopic determinations were performed using a procedure similar to that described by Bonhomme et al. (1975). Samples were pre-heated under vacuum at 80 °C for several hours to reduce the amount of atmospheric Ar adsorbed onto the mineral surfaces during sample handling. Argon was extracted from the separated mineral fractions by fusing samples within a vacuum line serviced by an on-line ^{38}Ar spike pipette. The isotopic composition of the spiked Ar was measured with a high sensitivity on-line VG3600 mass spectrometer. The ^{38}Ar spike was calibrated against international standard biotite GA1550 (McDougall & Roksandic, 1974). After fusion of the sample in a low blank Heine resistance furnace, the released gases were subjected to a two-stage purification procedure with a CuO getter for the first step, two Ti getters and a SORB-AC getter for the second step. Blanks for the extraction line and mass spectrometer were systematically determined and the mass discrimination factor was determined periodically by airshots. Ca. 20 mg of sample material was required for Argon analysis. During the course of the study, international standards HD-B1, LP6, GLO (Hess & Lippolt, 1994, Odin et. al. 1982), and airshots were analysed. The K-Ar ages were calculated using ^{40}K abundance and decay constants recommended by Steiger and Jäger (1977). The age uncertainties take into account the errors during sample weighing, $^{38}Ar/^{36}Ar$ and $^{40}Ar/^{38}Ar$ measurements and K analysis. K-Ar age errors are within 2-sigma uncertainty.

1.2 XRD methodology

The mineralogy of the various size fractions was determined by X-ray powder diffraction analyzis (XRD) using a Bruker D8 Advance XRD equipped with a Lynx-Eye Detector, and Co Kα radiation set at 35 kV and 35 mA.

Initial identification of minerals was made using EVA (Bruker Nano Inc.) software with comparison to reference mineral patterns using Powder Diffraction Files (PDF) of the International Centre for Diffraction Data (ICDD) and other available databases. Quantitative analysis of the pressed powder (PP) mounts was carried out using TOPAS (Bruker Nano Inc.), a PC-based program that performs Rietveld refinement (RR) of XRD spectra. Quantitative analyses appear reasonable when minerals in the samples can be matched to the standards. The lower the Goodness of Fit (GoF) value, the closer the standards match the unknowns and the better the results. Semi-quantitative analyses of the smear mounts are based on the Reference Intensity Ratio (RIR) method (EVA software; Bruker Nano, Inc.). The RIR method uses corundum as an internal standard such that the most intense X-ray peak for each mineral phase is compared to the 100% intensity corundum peak (i.e., I/Ic).

1.3 U-Pb carbonate geochronology

1.3.1 Sample Characterisation

Carbonate samples were cut and prepared into polished thick (80-100 µm thick) sections. Prior to analysis, sections were investigated using conventional optical polarized and reflected light microscopy to characterise carbonate and mineral inclusions. Subsequently, samples were imaged with Cathodoluminescence (CL) imaging using a CITL cold-cathode CL microscope at Kingston University, UK. All samples were CL-dark except sample 19A (Fig. 8 in this Data Repository) the imaging for the other samples was therefore not useful and is not presented in this manuscript. Carbonate chemistry was qualitatively characterised using EDS analysis using a ZEISS Evo MA 10 Scanning Electron Microscope at the University of Portsmouth (UoP), UK. Carbonate contains Ca, Fe and Mg so is likely dolomitic in composition. See U-Pb methods for details about potential matrix effects.

1.3.2 U-Pb analysis

U-Pb carbonate dating was performed at the University of Portsmouth, UK, using an ASI RESOlution© 193 nm ArF excimer laser coupled to a high sensitivity Jena Analytic PlasmaQuant Elite© LA-ICP-MS instrument. Carbonate was analyzed using 80 µm spot size, laser fluence of ≈2.5 J/cm2, and a repetition rate of 8 Hz. A 40um, 10 Hz, 4.5 Jcm2 line on NIST612 glass yields a typical sensitivity of ~1,000,000 cps U238 and a Hg202 background of 2000 cps. U/Th fractionation was typically ~0.95-1.05 and Th oxide production is <0.002. There was a 20 s background measurement, followed by 30 s of ablation, and 15 s of washout for each analysis. Four pulses of pre-ablation with a 90 µm spot size and a 15 s washout were used to clean the area before each analysis.

Prior to setting up an analytical run, 40 µm reconnaissance lines (run at 20 µm/ sec speed) and 40 µm 30-shot spots were briefly analysed to identify U-rich (1-10 ppm) areas of the carbonate crystals. Analysed spot locations can be found in the material below.

SRM612 glass (NIST612; 38 ppb U and Pb; Pearce et al. 1997) and WC-1 carbonate (254.4 ± 6.4 Ma; 5ppm U, >90% radiogenic; Roberts et al. 2017) were used as primary reference materials and Mudtank zircon (~12 ppm U, 732 ± 5 Ma; Black and Gulson, 1978; Jackson et al., 2004) was used as a secondary reference material to test long-term reproducibility. Analyzes of Mudtank during the analytical periods yielded a 206Pb/238U intercept age of 729 ± 4 Ma. Two of each reference materials were ablated between every 8 unknowns. The data were reduced and correcting for instrumental U-Pb drift, downhole fractionation (which was minimal/ non-existent), Pb isotope mass bias, U-Pb normalization and peak correction using NIST612 with Iolite© software (Paton et al. 2011). A second correction using an in-house spreadsheet was made using the WC-1 reference material to correct for the final matrix-matched normalization, and non-radiogenic Pb (Parrish et al. 2018; Appendix 3 for more information; average correction factor 1.08). 2 sigma uncertainties and include propagated analytical uncertainties, the reproducibility of WC-1 in each analytical session and a 5% uncertainty on the WC-1 RM have been added in quadrature to all data presented in data tables and in plots. Final quoted uncertainties include an additional 2% uncertainty added in quadrature to account for typical long-term reproducibility of analytical equipment. Any matrix effects caused due to differences between the dolomitic composition of analysed carbonate and the calcite composition of WC-1 is likely to be less than these additional added uncertainties. U-

Pb data are presented on Tera Wasserburg plots using Isoplot 4.15 (Ludwig, 2003) with non-common Pb corrected intercept ages reported with 2σ uncertainties.

Table 1: LA-ICP-MS operating conditions

Laboratory & Sample Preparation	
Laboratory name	School of Earth and Environmental Science at the University of Portsmouth
Sample type/mineral	Carbonate
Sample preparation	Fragments of rock with veins, 1'' epoxy mount, 1µm polish to finish Thick sections
Imaging	Reflected light image and CL imaging for some samples
Laser ablation system	
Make, Model & type	ASI RESOlution SE ArF (Argon-Fluoride)
Ablation cell & volume	Laurin S155 (dual volume design)
Laser wavelength (nm)	193nm
Pulse width (ns)	3 ns
Fluence (J.cm^{-2})	2.5 J/cm^2
Repetition rate (Hz)	8 Hz
Spot size (um)	80µm following 90µm pre-ablation of 4 pulses
Sampling mode / pattern	Spot, with pre-ablation cleaning spot
Carrier gas	100% He (0.31 l min$^{-1)}$, Ar make-up gas (0.9 l min^{-1}) combined 50% along sample line in mixing bulb
Ablation duration (secs)	30 secs, 15 s washout, 20 s background between pulses
Cell carrier gas flow (l/min)	100% He (0.310 l/min), N2 (0.0031 l/min)
ICP-MS Instrument	
Make, Model & type	PlasmaQuant MS Elite (quadrupole) from Analytik Jena
Carrier gas flow rate	0.32 l min^{-1} He and 0.9 l min^{-1} Ar
Auxilary gas flow rate	1.65 l min^{-1} Ar
RF power (W)	1300 W
Detection system	3 MHz quadrupole
Masses measured	^{202}Hg, ^{204}Hg + Pb, ^{206}Pb, ^{207}Pb, ^{208}Pb, ^{232}Th, ^{235}, ^{238}U
Integration time per peak (ms)	10-15ms
Data Processing	
Gas blank	20 second on-peak zero subtracted
Calibration strategy	SRM612 used as primary reference material for downhole corrections, mass fractionation for Pb, and U-Pb drift correction and U-Pb initial normalization; WC-1 was used for carbonate for final U-Pb calibration
Reference Material info	SRM612 glass and 254.4 ± 6.4 Ma WC-1 for final Pb/U calibration Mud Tank zircon, 732 Ma
Data processing	Iolite© 3.4 software, using the 'Linear spline' to correct for downhole

package used / Correction for LIEF	fractionation and the 'Automatic spline' to correct for instrumental drift
Common-Pb correction, composition and uncertainty	using Excel spreadsheet using both ^{207}Pbc and ^{208}Pbc methods (described in Parrish *et al.* 2018, supplementary material); Measurements of SRM612 glass, WC-1 and Mud Tank zircon were done along with samples throughout all analytical sessions. **Propagated analytical uncertainties:** analytical uncertainties, reproducibility of WC-1 in each analytical session and a 5% uncertainty on the WC-1 RM have been added in quadrature to all data presented in data tables and in plots. Final quoted uncertainties include an additional 2% uncertainty added in quadrature to account for typical long-term reproducibility of analytical equipment

1.3.3 Standard reproducibility

Table 2: Standard reproducibility

Conditions							uncorrected WC-1		WC-1	corrected WC-1		Mudtank		
Sample	Date	run	Spot size	power (mJ)	Hz	Primary	Intercept	uncertainty	Correction factor	Intercept	uncertainty	WA	uncert	reproducibility
17A	231118	2	80	2.5	8	NIST612	273.8	3.3	1.078	254.3	3.1	718.2	3.3	1.93
19A	231118	2	80	2.5	8	NIST612	273.8	3.3	1.078	254.3	3.1	718.2	3.3	1.93
542B	281118	3	80	2.5	8	NIST612	279.4	3.4	1.100	254.3	3.1	695	4.9	5.09
548A	281118	3	80	2.5	8	NIST612	279.4	3.4	1.100	254.3	3.1	695	4.9	5.09
542D	31218	1	80	2.5	8	NIST612	278.9	2.9	1.098	254.3	2.7	694.3	6.5	5.19
548B	31218	1	80	2.5	8	NIST612	278.9	2.9	1.098	254.3	2.7	694.3	6.5	5.19
542A	41218	1	80	2.5	8	NIST612	266.9	2.9	1.051	254.1	2.8	732	7.2	0.04
542C	41218	1	80	2.5	8	NIST612	266.9	2.9	1.051	254.1	2.8	732	7.2	0.04
Average									1.082	254.4	1.5	708.6	3.3	3.24

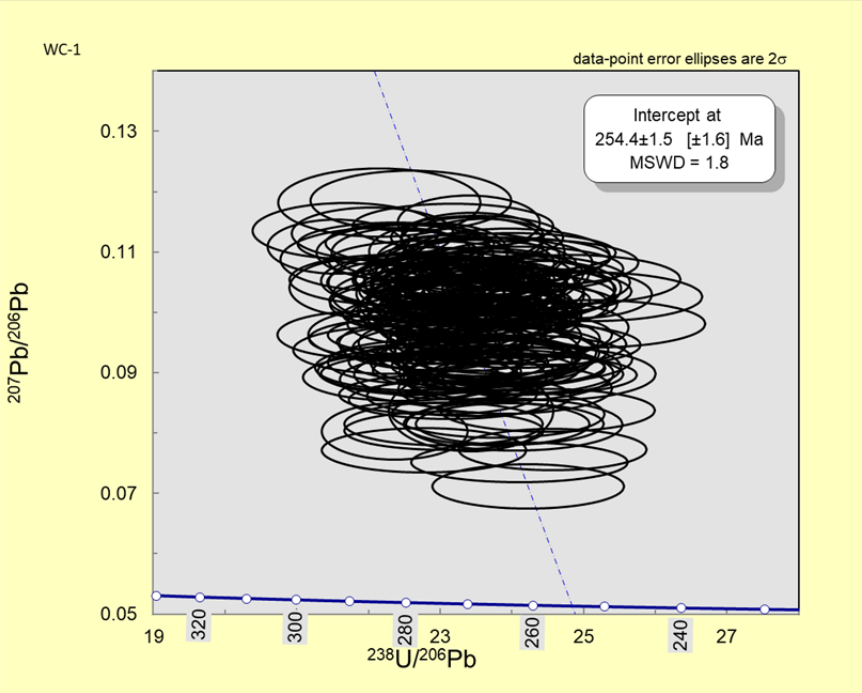

Figure 1: Tera Wasserburg plot of all corrected WC-1 analyzes for all analytical sessions (non-corrected data included in Table 2

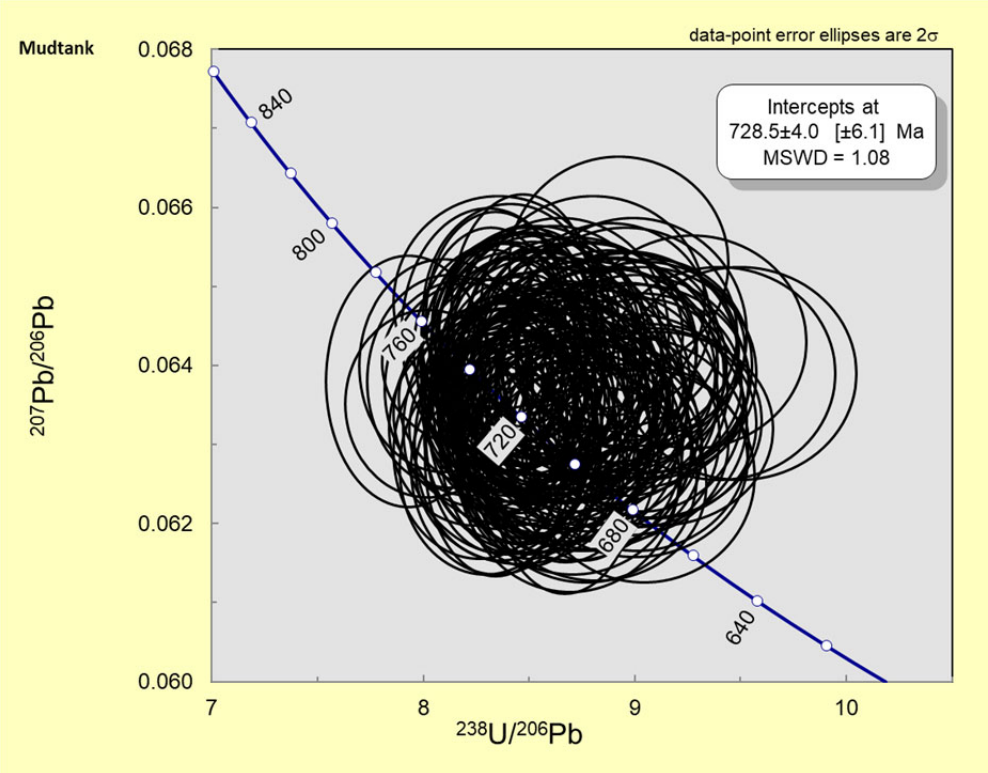

Figure 2: Tera Wasserburg plot of all Mudtank analyzes for all analytical sessions (Table 2)

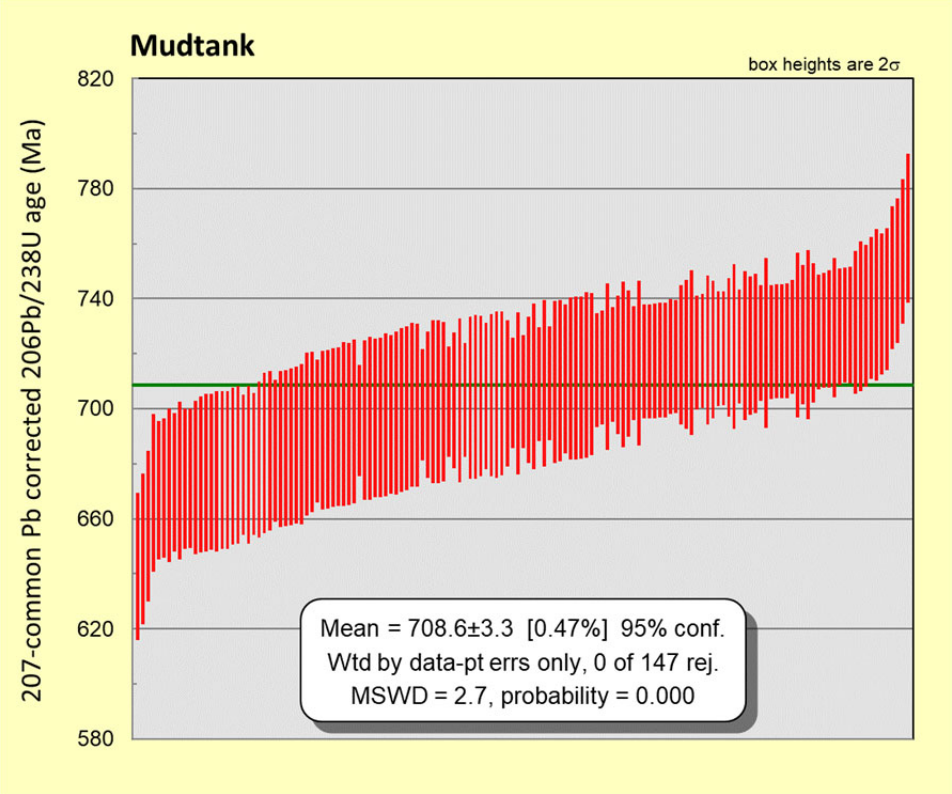

Figure 3 U/Pb weighted average of all Mudtank analyses for all analytical sessions (Table 2)

2. Fault gouge sample descriptions

Sample	Lat	Long	Notes
Seymour Creek	62.31029 °N	137.20890 °W	Several narrow gouge zones cut through fractured and highly altered Stoddart Creek monzonite were temporarily exposed from beneath thick river gravels and sands in workings of a placer operation in Stoddart Creek. Gouge zones have general NW-SE strike and ~60° dip. Sampled gouge zone is 20 cm wide seam of orangey-brown clay with fault walls oriented 097°/75°. No obvious offsets or kinematics. Some slickenlines, but difficult to measure in place, and no mineral growth on surfaces.
Mechanic Creek	62.33398 °N	137.31621 °W	Gouge was sampled from a 5 m wide sub-vertical gouge zone of white-grey and brown gouge bounded by intensely silica-altered wall rock trending at 150˚/330° within Whitehorse suite granodiorite. An adjacent and parallel gouge seam is 10 m wide.
Happy Creek	62.33956 °N	137.23584 °W	Gouge was sampled from a stream outcrop of 20 cm wide yellow-grey gouge oriented ~173°/74° hosted in Paleozoic layered schist/gneiss

Blue Sky Porphyry Breccia (RVD-18-21)	62.33166°N	137.25294°W	Fault gouge clay was sampled from the 557.26-558.40 m interval within brecciated granodiorite. Abundant sulphide-bearing (mostly pyrite) calcite veins above, and sampled calcite slickenfibres beneath the gouge interval.

3. Calcite sample descriptions

Table 3: Summary of all analyzed calcite samples, U content and U-Pb date (if successful)

Core all DDH	Depth (m)	Description	Orientation	Carbonate sample	Dated (Ma)	Average U (ppm)	Minimum U (ppm)	Maximum U (ppm)
RVD18-17	282.5	Slickenfibres	Not oriented	17A	Not successful	0.3	NA	NA
RVD18-17	437.1	Slickenfibres	Not oriented	17B	Not successful	<0.1	NA	NA
RVD18-19	314.06	Slickenfibres on fracture cross cutting Quartz-feldspar porphyry dyke	Not oriented	19A	56.8 ± 1.2 [± 1.7 prop] (MSWD 2.6, n=42)	9.7	1.7	32.4
RVD18-21	542.44	Mineralized vein	239/73	542A	72.8 ± 1.1 [± 1.7 prop] (MSWD 1.8, n=39)	6.0	1.0	14.8
			239/73	542B Blocky	72.6 ± 3.1 [± 3.4 prop] (MSWD 2.4, n=15)	6.3 0.5	1.1 0.2	17.3 0.6

				vuggy	57.8 ± 5.9 [± 6 prop] (MSWD 2.8, n=22)			
			239/73	542C vuggy	60.3 ± 2.3 [± 2.6 prop] (MSWD 3.1, n=22)	2.3	0.6	9
			239/73	542D vuggy	59.1 ± 2.4 [± 2.7 prop] (MSWD 2.2, n=40)	2.9	0.2	19.9
	548.44	Mineralized vein	242/65	548A vuggy	58.1 ± 1.8 [± 2.1 prop] (MSWD 1.9, n=44)	3.0	0.05	6
			242/65	548B vuggy	54.8 ± 6.4 [± 6.5 prop] (MSWD 3.7, n=29)	0.3	0.08	1.3
	557.26-558	Cataclasite and grey fault gouge	~N-S	K-Ar gouge	58.7±1.4, 57.2±1.3 and 44.4±1.1 Ma			
	566.24	Slickenfibres	Not oriented	21A	Not successful	<0.1	NA	NA

All samples were collected from Diamond Drill Hole Core (DDH)

3.1 DDH RVD18-19, 314.06 m slickenfibre sample (19A)

Figure 1: RVD-18-19 @ ~310-314 m quartz-feldspar porphyry dyke cross cut by fractures with slickenfibres

General Host rock: The samples in core RVD18-19 come from biotite granodiorite with subhedral feldspars throughout and similar to the Revenue granodiorite seen locally through the Revenue area. The granodiorite is cut by buff-coloured Quartz-Feldspar-Porphyry (QFP) dykes (Fig. 4) at two intervals in this core: 310.77-316.28 m and 462.65-476.96 m. Both QFP are characterized by medium-grained feldspar porphyry with distributed quartz

eyes and euhedral Kspar xenoliths up to 1 cm in size. The groundmass is fine-grained alteration sericite. The QFP crosscuts the granodiorite with thin chilled margins. The QFP dyke from 310.77-316.28m is crosscut by ~1 cm wide "V3" quartz-chalcopyrite-carbonate dykes and thin <1 mm quartz, carbonate and sulphide "stringers" and fractures with fine chlorite-carbonate slickenfibres. At ~311.90 m there is a triangular-shaped ~2 cm across chalcopyrite- quartz infill in the QFP dyke similar to breccia fill seen elsewhere in the Bluesky breccia. At ~318 m there is a rubbly gouge zone possibly representing a small fault surface that the fractures and slickenfibres could be related to. As this core was not oriented it is not possible to know the regional orientation of this structure. The lower QFP dyke is fractured and has minor mineralized stringers but no veining, slickenfibres or breccia fill.

Slickenfibres:

This sample is a fracture within a QFP dyke with intergrown chlorite-carbonate slickenfibres on the surface. Slickefibres form a <1 mm thick veneer (Figure 5) and there are some poorly defined steps but with unresolvable sense of motion due to unoriented core. In thin section, the sample has several shear surfaces within the QFP dyke (Figure 5) indicating that fracturing occurred on multiple surfaces. Analyses were conducted along the length of the slickenfibre (Figure 6).

Figure 2: Sample RVD18-19-314 "19A" in hand specimen

DDH RVD18-19, 314m ("19A")

Figure 3: Sample RVD18-19-314 "19A" showing analysed portion of the material (highlighted in yellow).

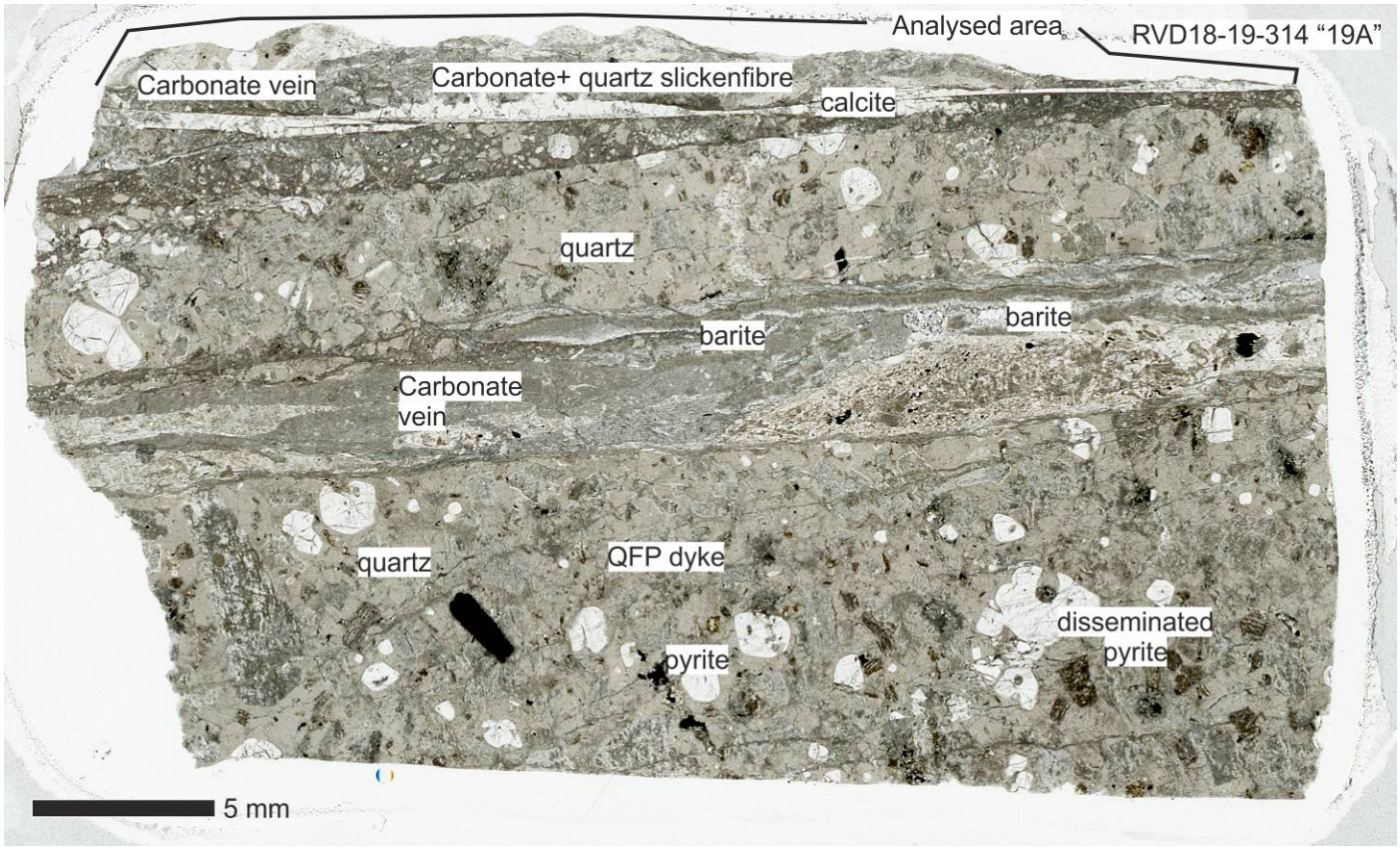

Figure 4: RVD18-19-314 “19A” with key minerals annotated

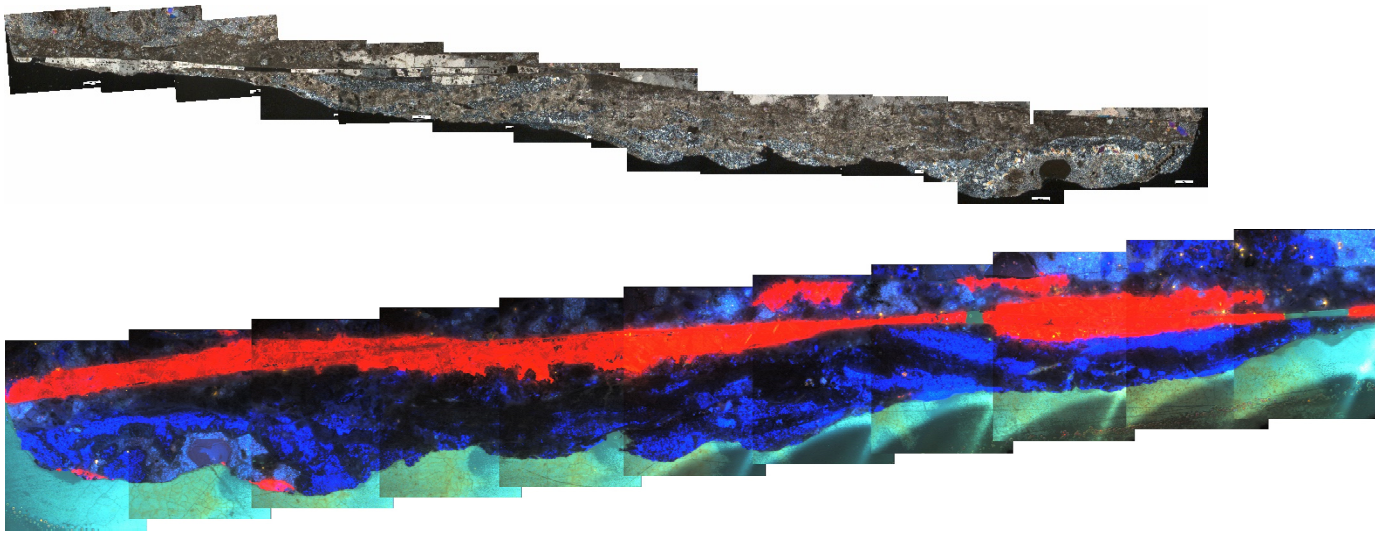

Figure 5 Stitched XPL-polar photomicrograph of sample RVD18-19-314 “19A” and stitched CL image

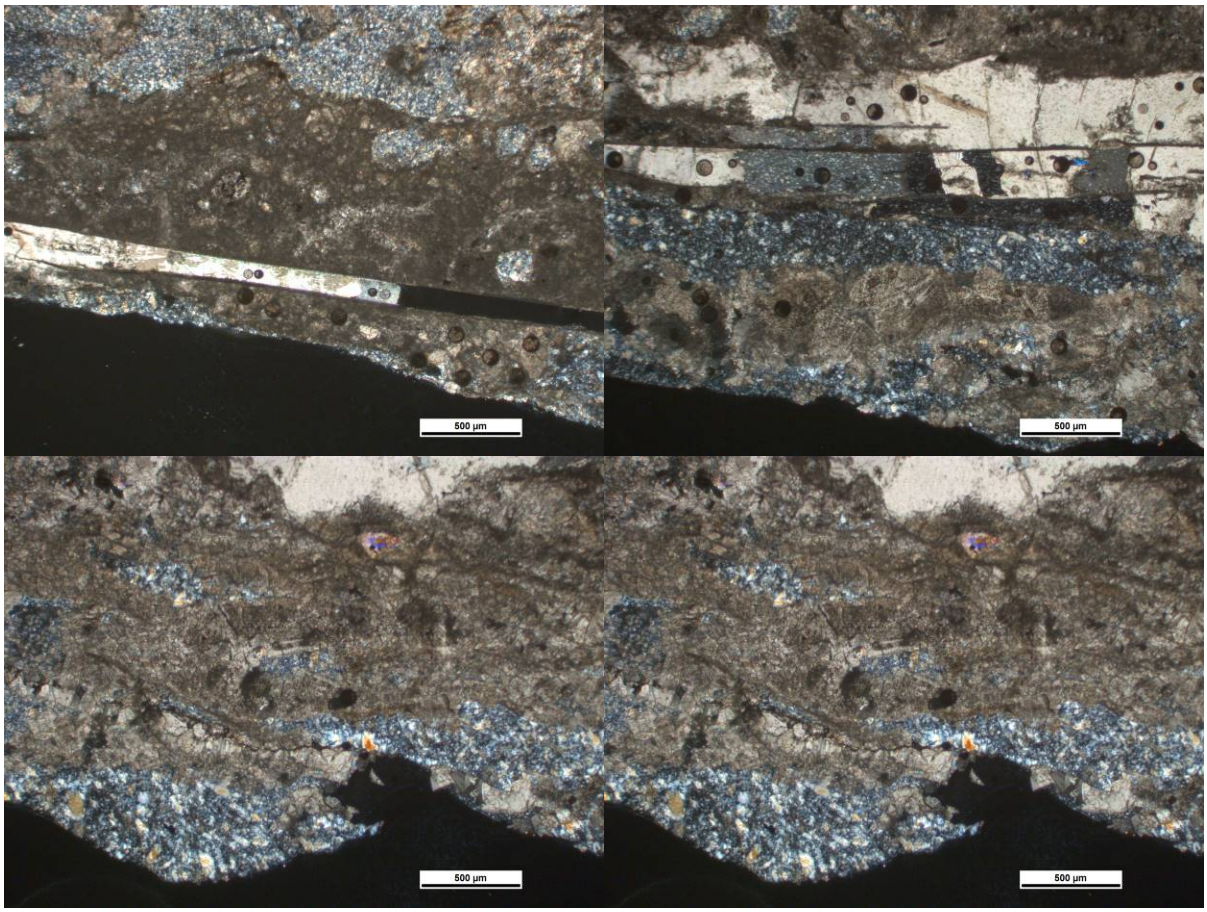

Figure 6: XPL photomicrograph of sample RVD18-19-314 "19A"

3.2 DDH RVD18-21, 530- 560 m

General Host rock: This section of core is a dark grey to black to altered greenish-grey medium-grained biotite-hornblende (bio-hbl) granodiorite with 35% feldspar, 40% quartz, 15-20% K feldspar, 5-10% 2-5 mm biotite and 5% hornblende. Throughout this section the core is intact with 4-5 NE-SW striking cross cutting multi-layered grey-pink quartz-carbonate-sulphide veins striking 239/73 (RHR) and 242/65 (RHR) for 542m and 548 m respectively. Between 553.07-559.31m there is a rubbly fault zone that is dominated by cataclasite and grey fault gouge. Due to the rubbly nature of the core orientation measurements are challenging to take, however the upper fault contact was measured at 006/66 (RHR) and 035/35 (RHR) for a fault fabric within the fault zone.

Figure 7: RVD-18-21 ~542-546m medium grained granodiorite cross cut by mineralized carbonate veins

DDH RVD18-21, 542m

This NE-SW (239/73) striking, high angle vein has several layers- a whitish grey 5 mm carbonate vein with a pyrite selvage on one side, a ~1-1.5 cm thick concordant pinkish vuggy carbonate layer that is concordant with a 5 mm thick zone of fine grained quartz/chalcedony and additional pyrite and carbonate veins (Figure 8). All veins are oriented 239/73 (Figure 10-11).

Figure 8: Hand specimen photographs of RVD18-21-542m layered carbonate vein

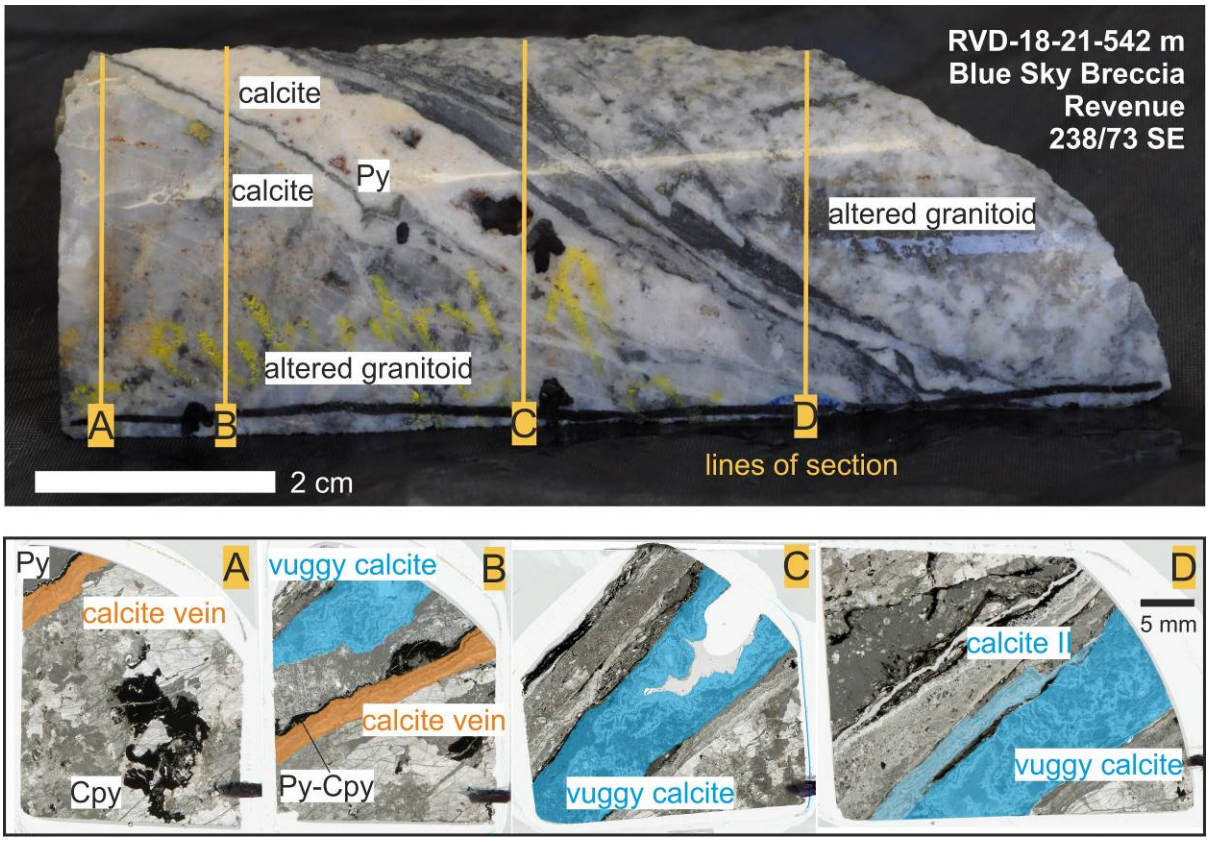

Figure 9: Hand specimen of sample RVD18-21-542m that has been cut into 4 sections though the layered carbonate vein. Thin section images A-D show the different characteristics between the thin (~5 mm) crustiform carbonate with pyrite crust (highlighted in orange), and the thicker vuggy calcite and other secondary calcite veins (highlighted in blue).

542A thin section characterization

Section 542A is comprised of altered granitoid with disseminated pyrite and chalcopyrite (Figure 14). At the top of the section is a ~3 mm thick carbonate vein, where euhedral rhomboid crystals form a elongate-blocky vein texture. It can be interpreted that the carbonate crystals grew from the wall altered granitoid. A layer of pyrite encrusts the edge of the carbonate vein, with carbonate crystals euhedrally in contact with the pyrite which can be seen to wrap around the carbonate (Figure 15). These textures can be interpreted to suggest that pyrite grew either at the same time as the carbonate or was (re)mobilized and (re)crystallized at the edge of the vein.

Figure 10: Section RVD18-21-542A Analysed portion of crustiform vein is highlighted in yellow

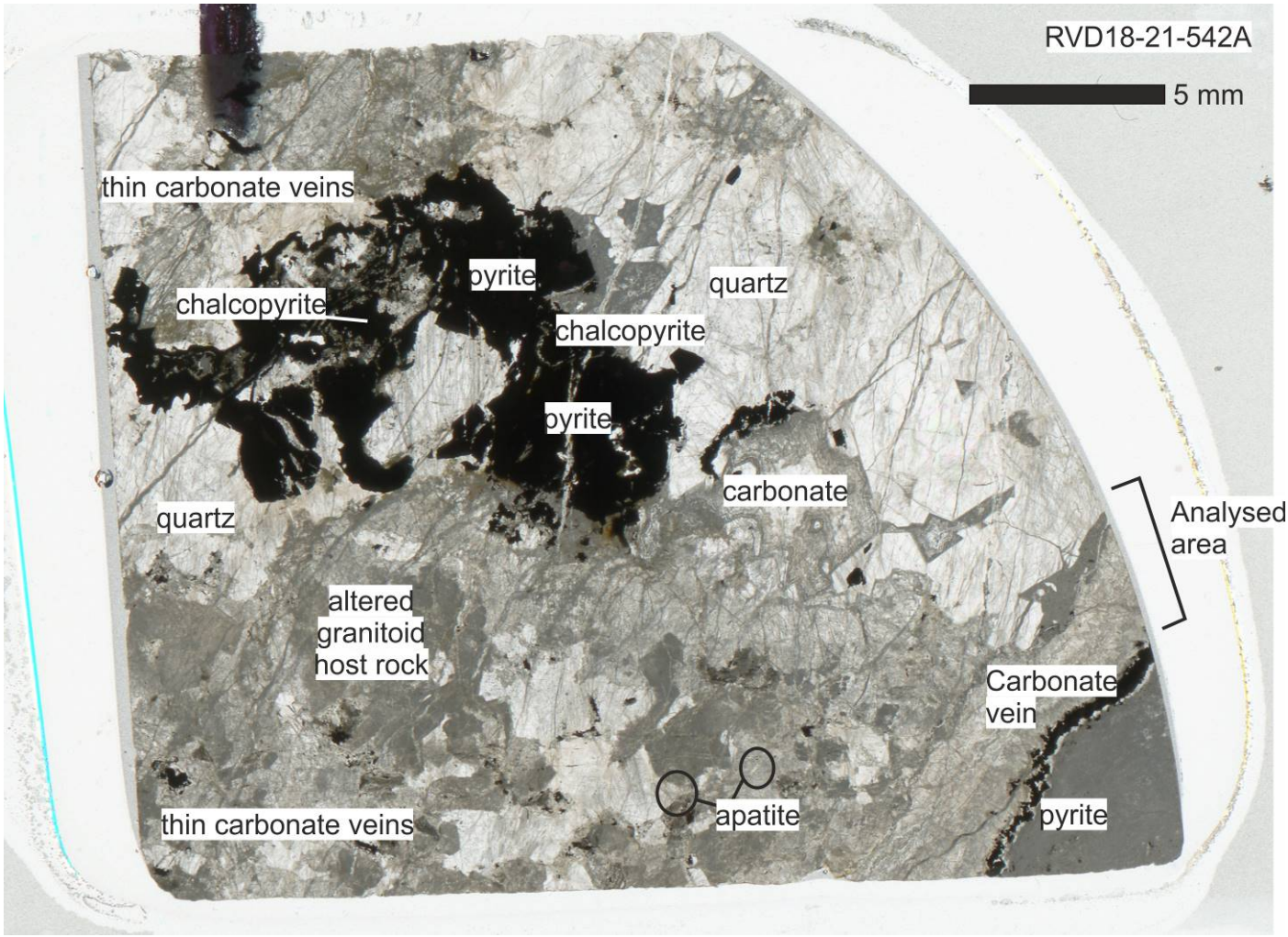

Figure 11: RVD18-21-542A with key minerals annotated

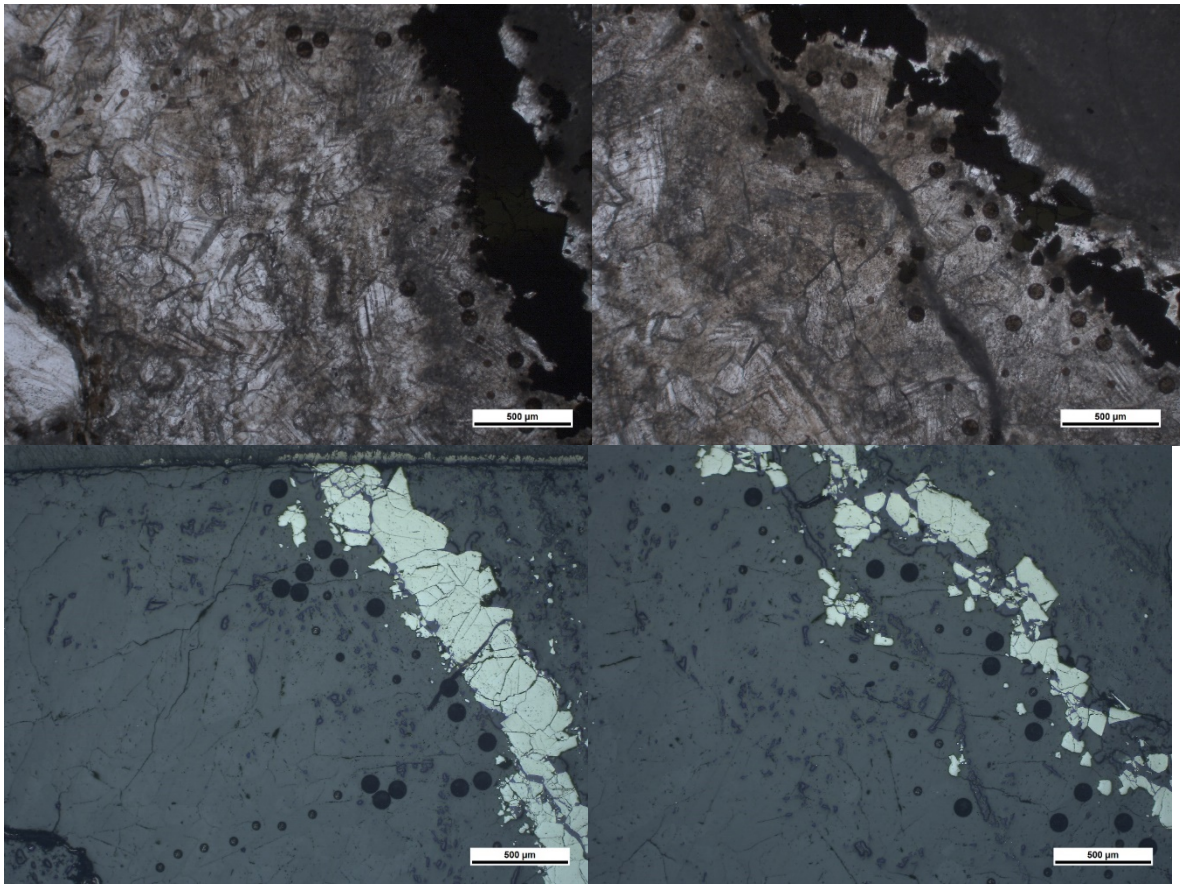

Figure 12: XPL and reflected light images of crustiform carbonate in sample RVD18-21-542A

542B thin section characterization

Section 542B is an altered granodiorite with disseminated pyrite. This granitoid is cut by two carbonate veins. (1) In similarity with 542A, a ~3 mm carbonate vein shows euhedral-elongate-blocky textures (Figures 16-17). This texture can be interpreted as carbonate growth from the wall rock. The carbonate is encrusted with pyrite and the carbonate and pyrite can be seen to be intergrown (Figure 18). (2) There is a massive (1.5 cm thick) vuggy carbonate vein with euhedral minerals (Figure 17, 19). These crystals can be interpreted to have grown from the walls into the centre of the vein where there are voids.

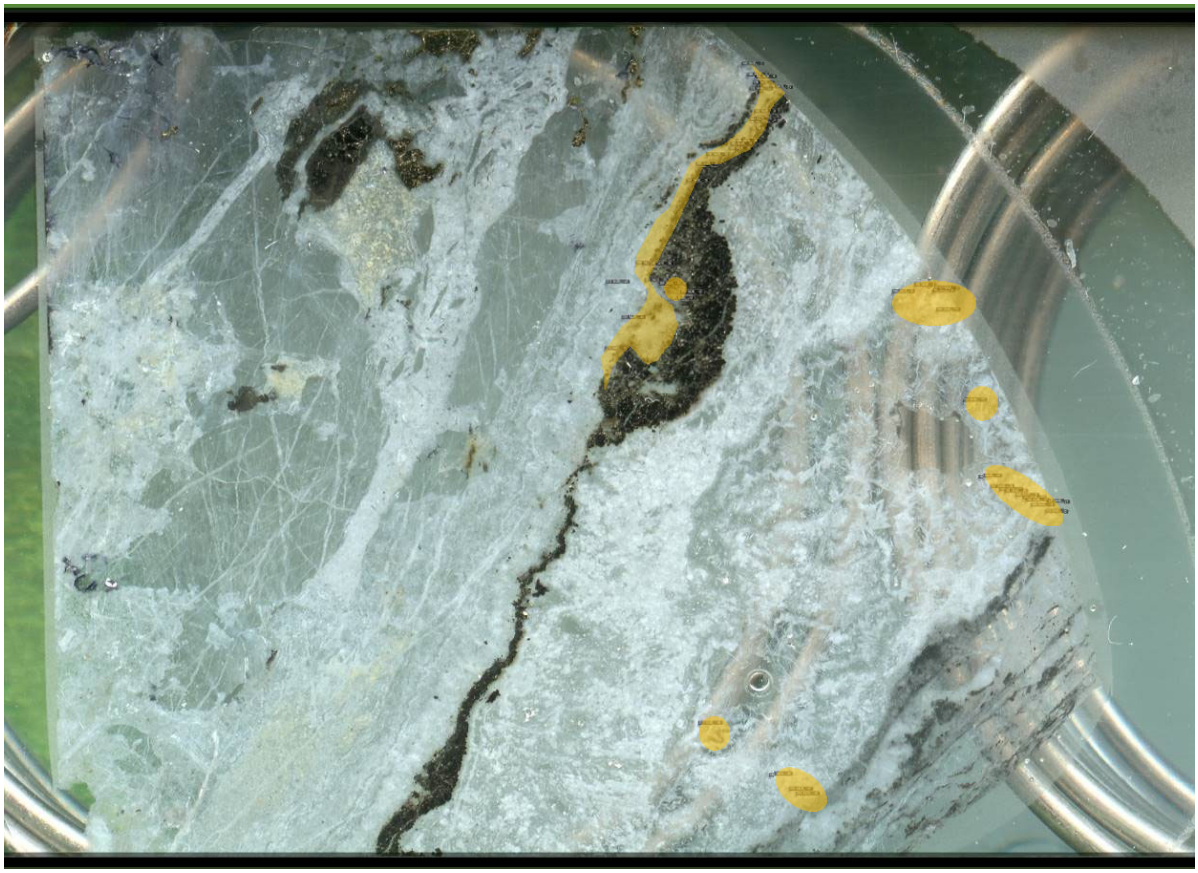

Figure 13: Section RVD18-21-542B Analysed portion of crustiform vein and vuggy carbonate is highlighted in yellow

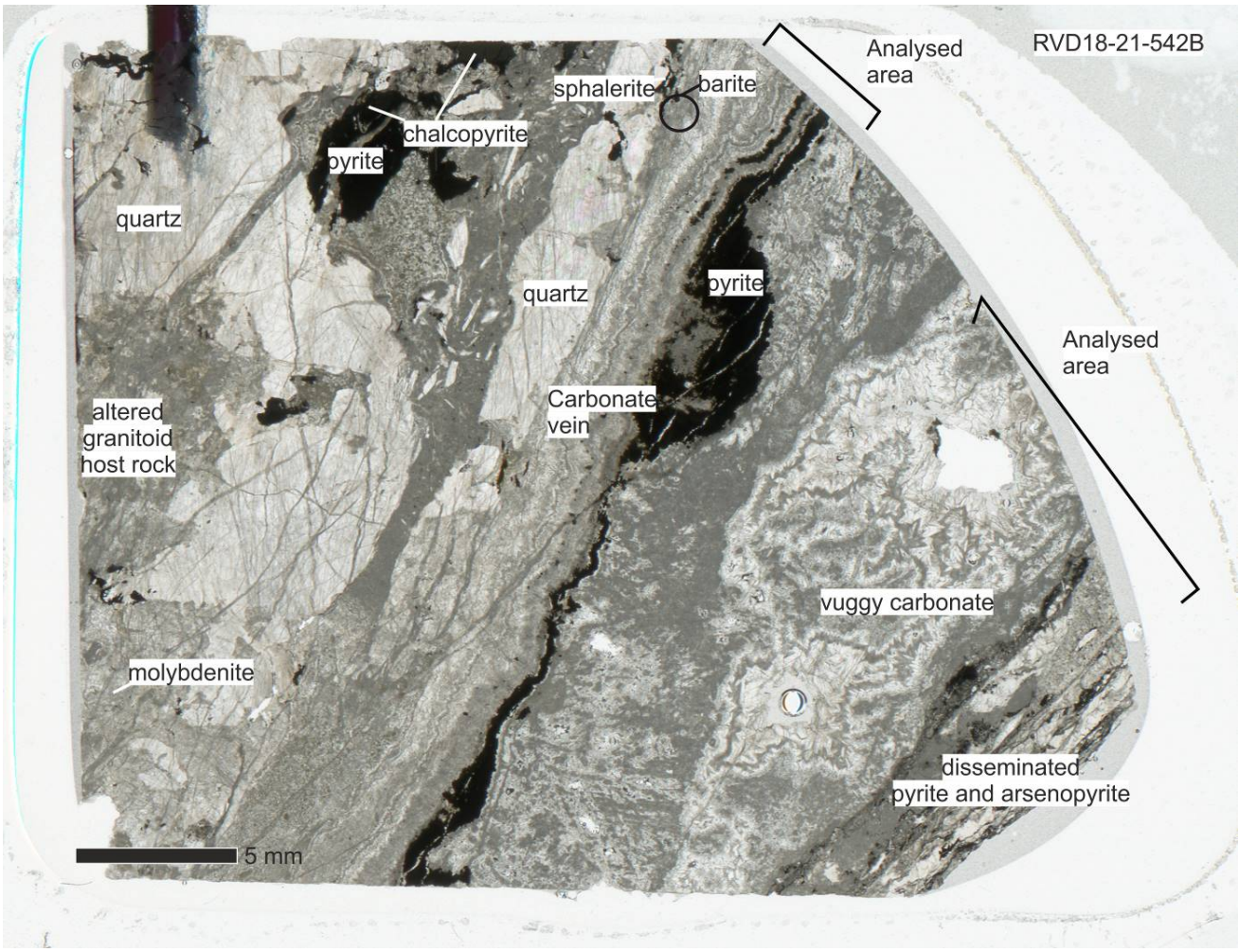

Figure 14: RVD18-21-542B with key minerals annotated

542B thin section characterization

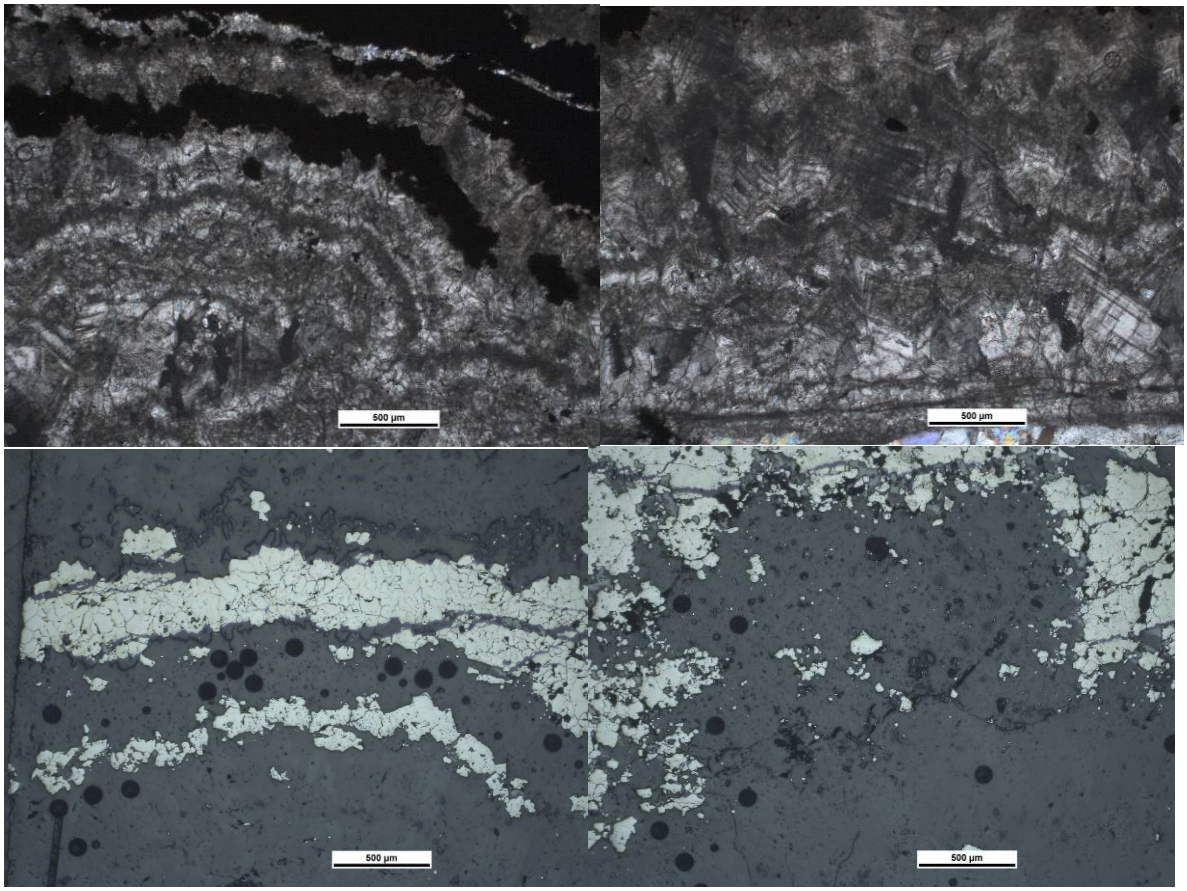

Figure 15: X-polarized and reflected light images of crustiform carbonate in sample RVD18-21-542B

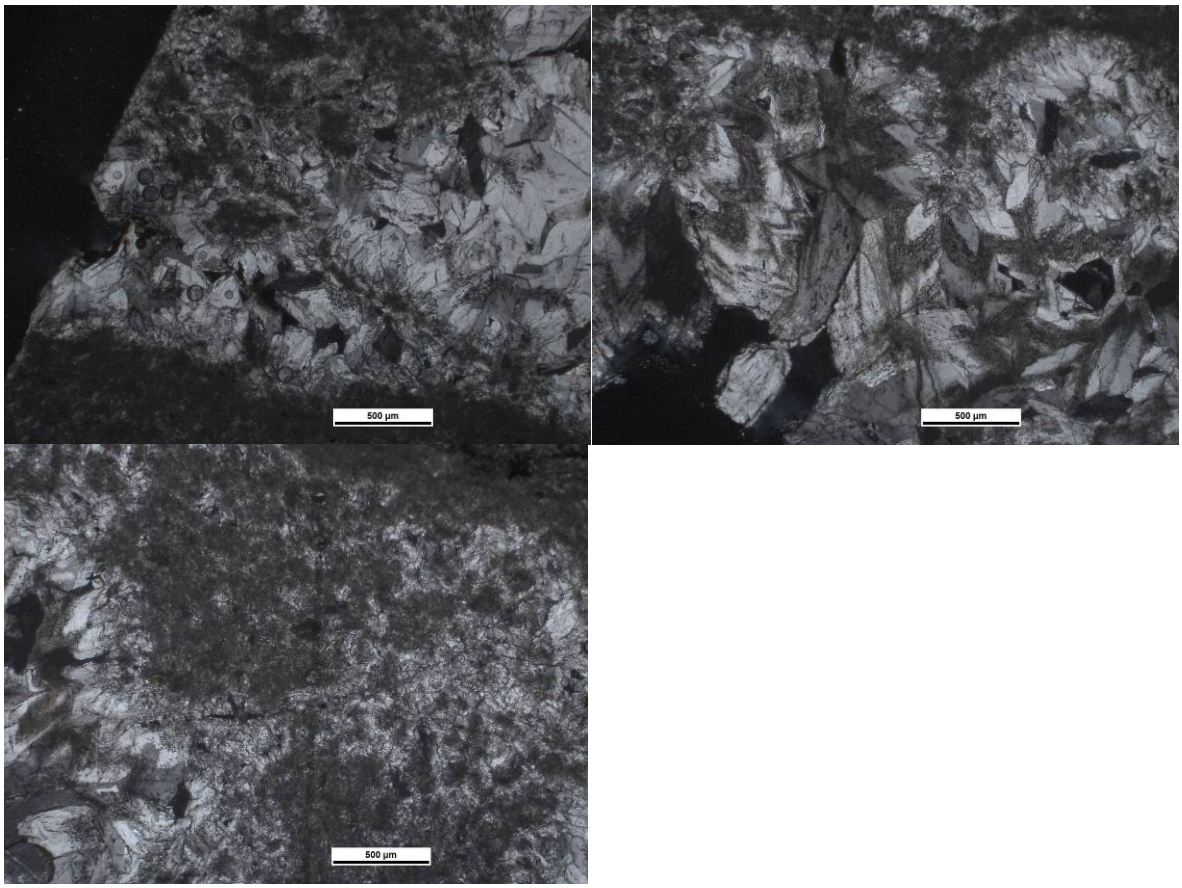

Figure 16: X-polarized and reflected light images of vuggy carbonate in sample RVD18-21-542B

542C thin section characterization

Section 542C is altered granitoid wall rock, cross cut by the ~1.5 cm thick vuggy carbonate vein (2) described in section 542C (Figure 20-21). The walls of this vein have a finer-grained carbonate and crystal size increases to ~1-2 mm in the centre of the vein which also contains voids (Figure 21). Intergrown with the larger carbonate crystals are very fine-grained carbonate (Figure 22). Both the coarse and fine-grained carbonate were analysed (laser spots can be seen in Figure 22). The edges of the vein are concordant with very fine-grained silica that can be interpreted as a small fault zone.

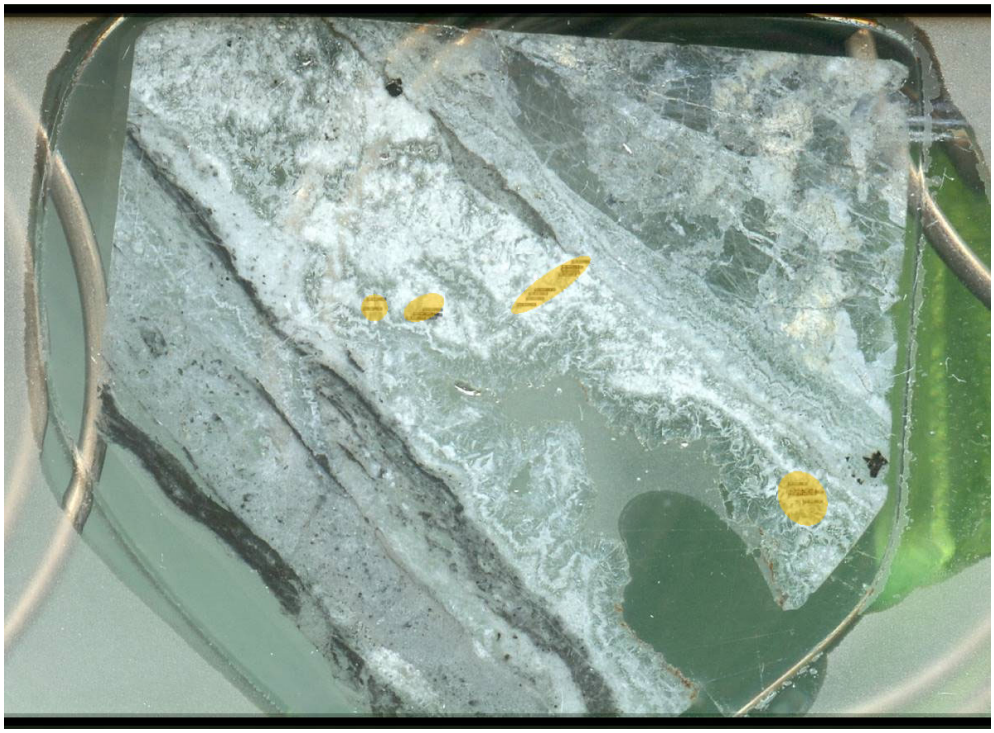

Figure 17: Section RVD18-21-542C Analysed portion of vuggy carbonate is highlighted in yellow

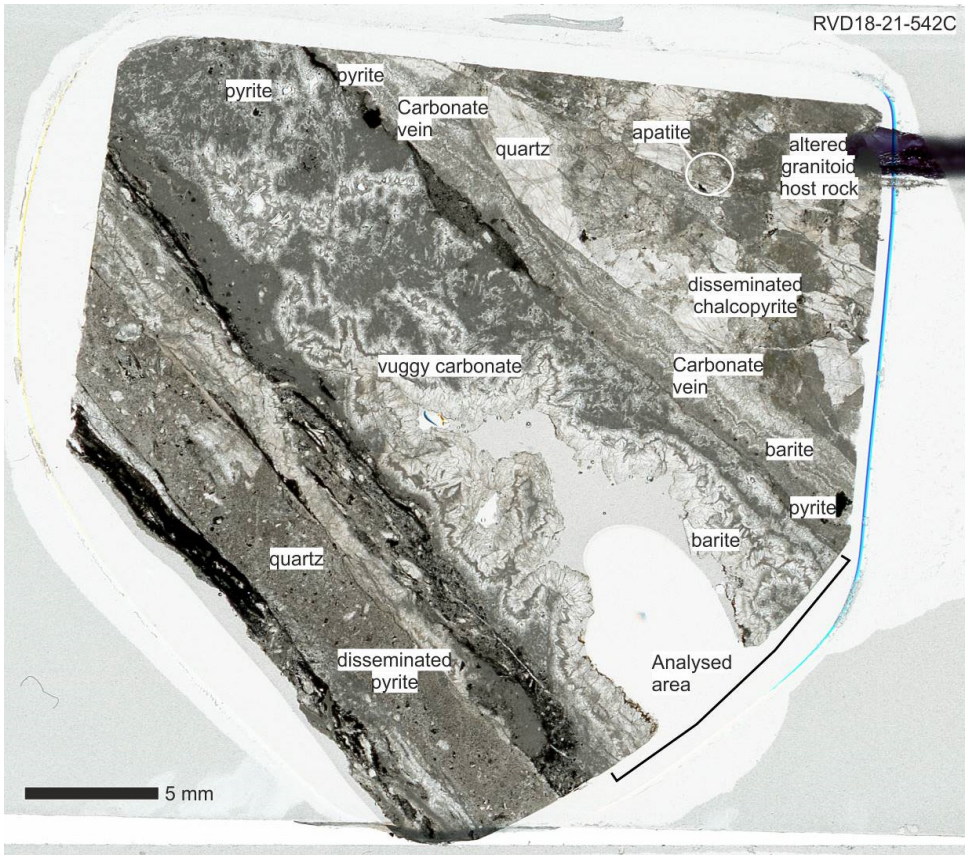

Figure 18: 542C

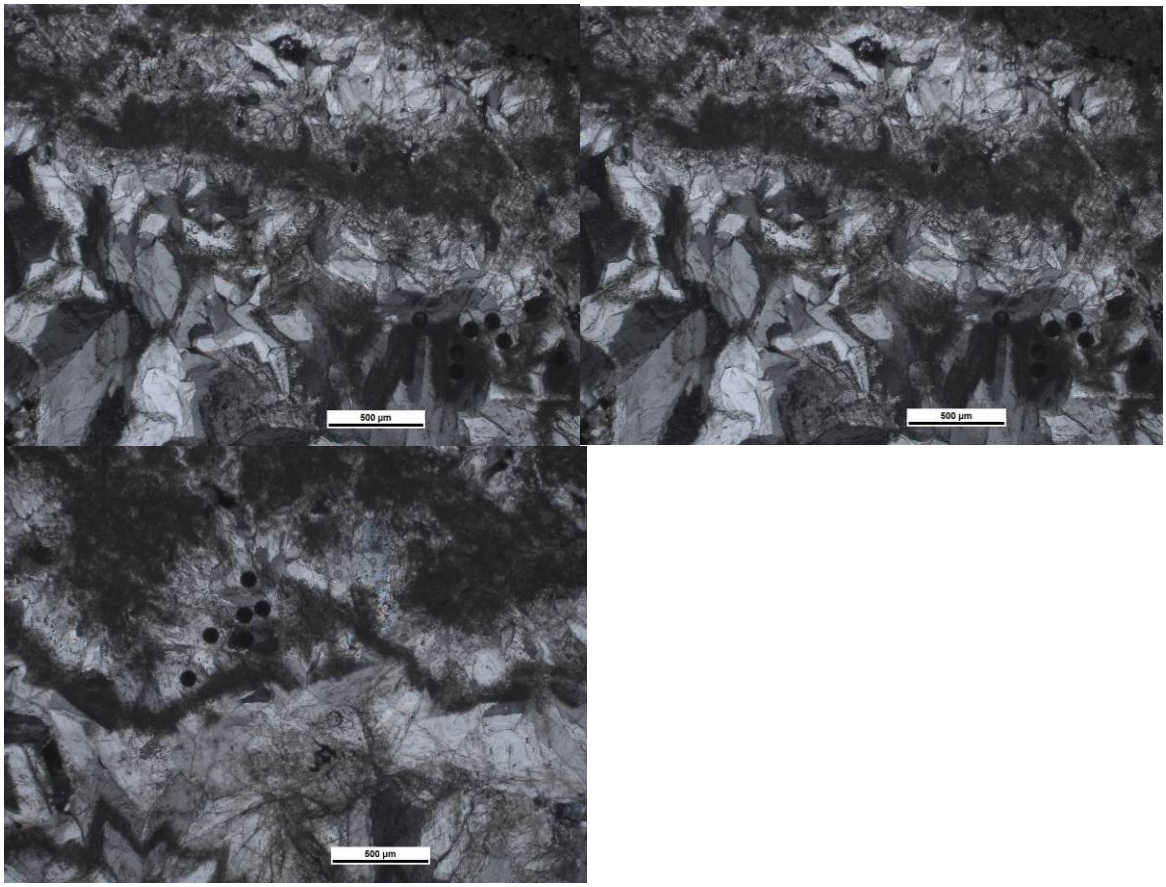

Figure 19: X-polarized light images of vuggy carbonate in sample RVD18-21-542C

542D thin section characterization.

Section 542D has altered granitoid at the edges. The centre of the section is dominated by a seemingly multi-layered carbonate vein (Figure 23-24). There is a vuggy vein ~1 cm thick with the characteristic textures displayed in section 542B and C in vein (2; Figure 24, 26). Concordant with this are several other carbonate veins ~3-5 mm thick separated from one another by very fine-grained silica (Figure. 25). Both the vuggy vein (2) and the other carbonate veins were analyzed, including part of a vein that has a pyrite crust (Figure 25).

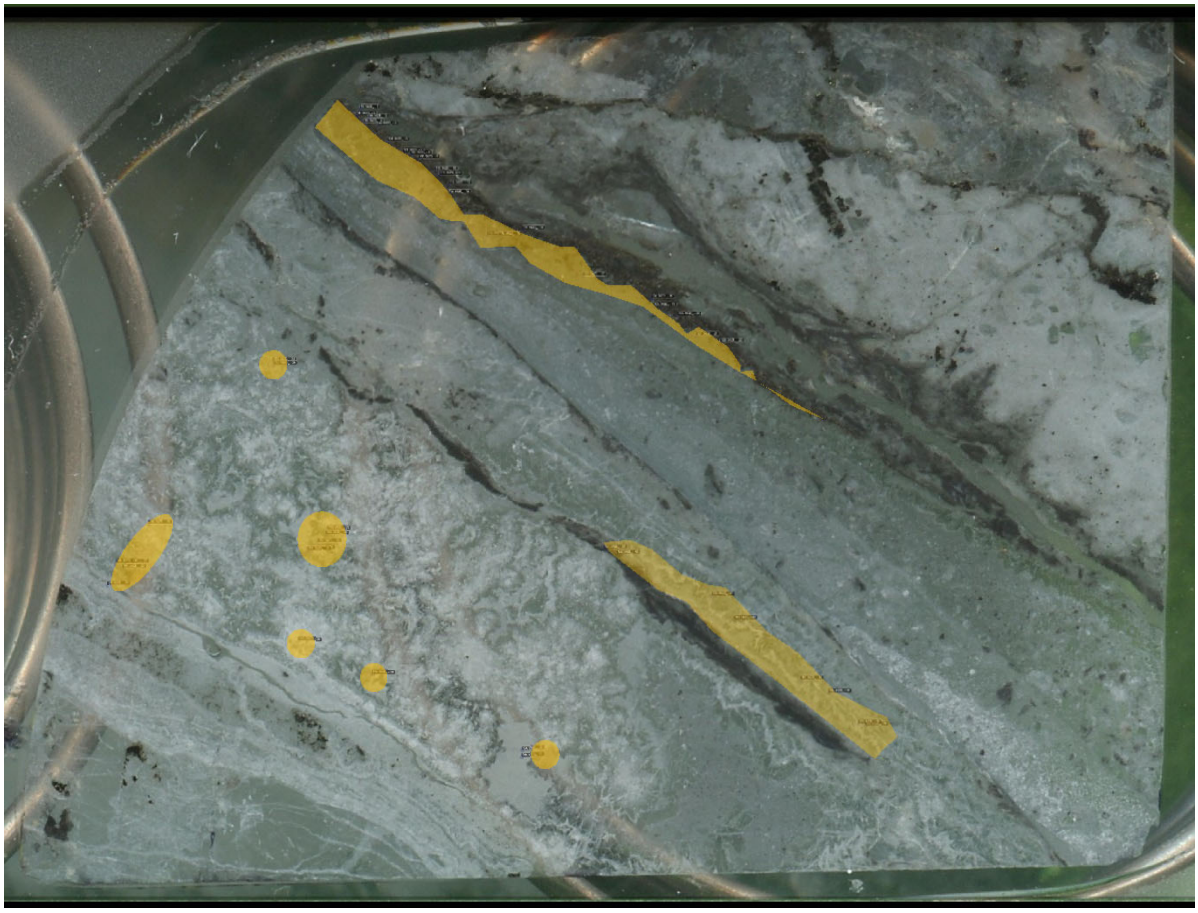

Figure 20 Section RVD18-21-542D Analysed portion of vuggy and secondary carbonate is highlighted in yellow

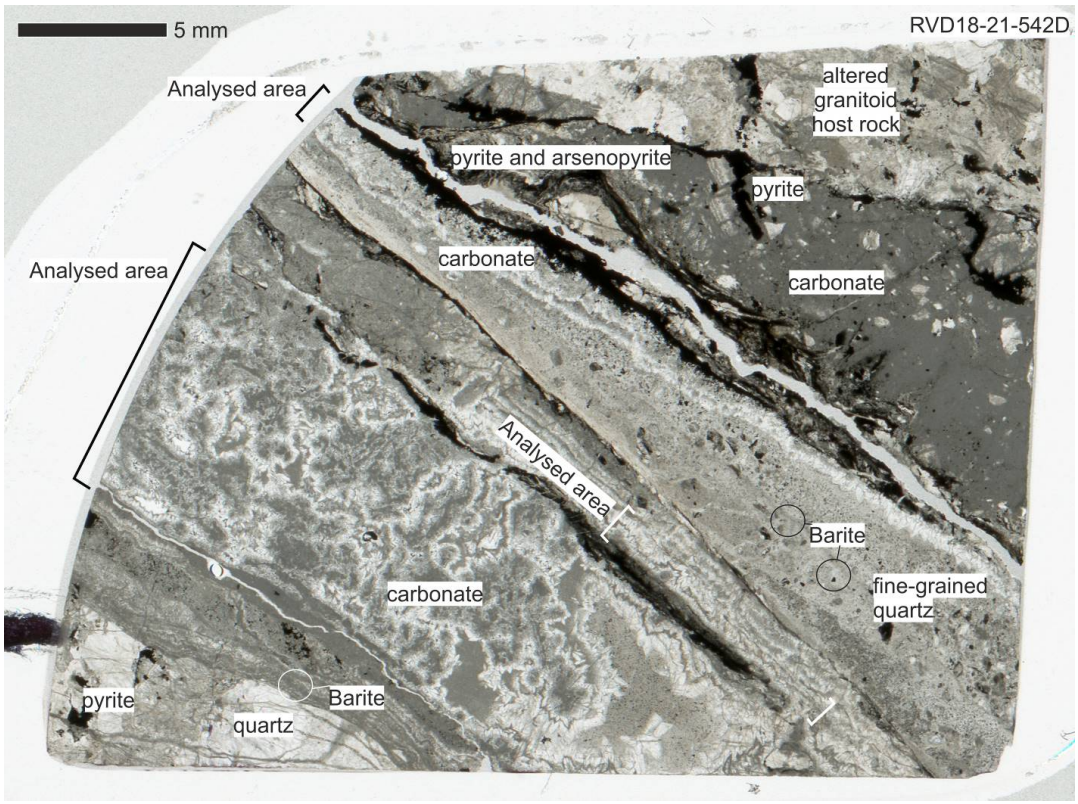

Figure 21: RVD18-21-542D with key minerals annotated

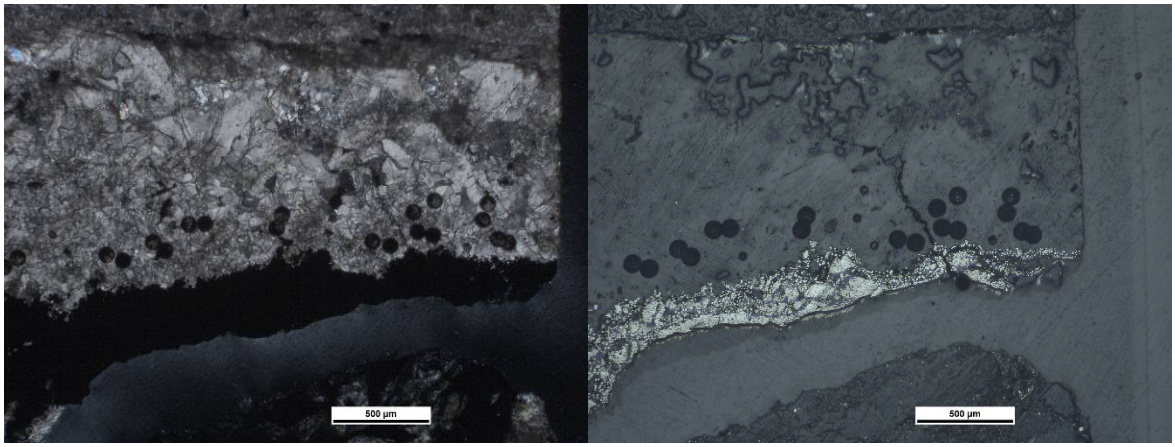

Figure 22 X-polarized and reflected light images of secondary carbonate veins in sample RVD18-21-542D

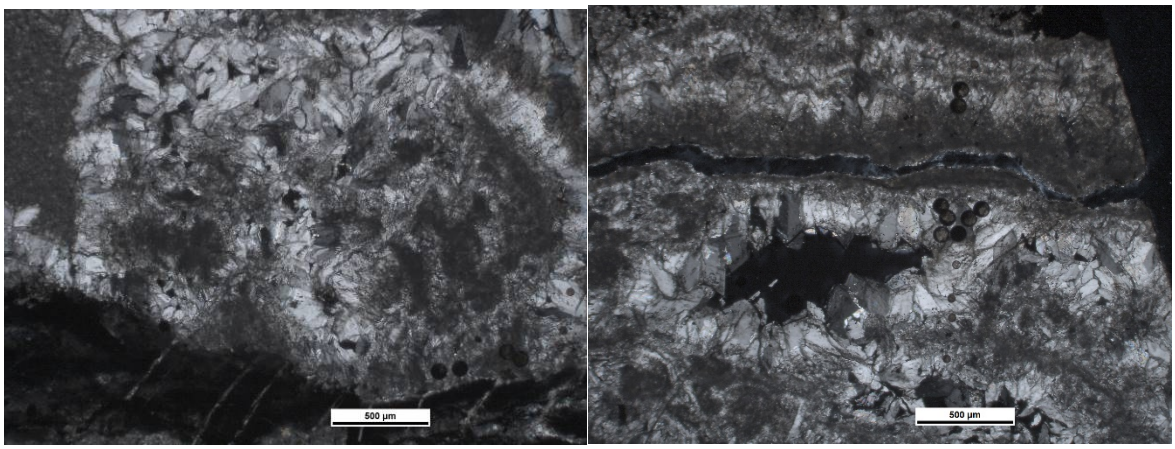

Figure 23: X-polarized images of vuggy carbonate veins in sample RVD18-21-542D

DDH RVD18-21-548 general description

On a hand specimen level, this NE-SW striking, high angle vein has several layers- a pinkish straight 2 mm carbonate with a pyrite crust concordant with a ~1cm grey fine-grained brecciated vein. This material has a matrix of very fine-grained silica separating fragments of quartz with a carbonate in-fill

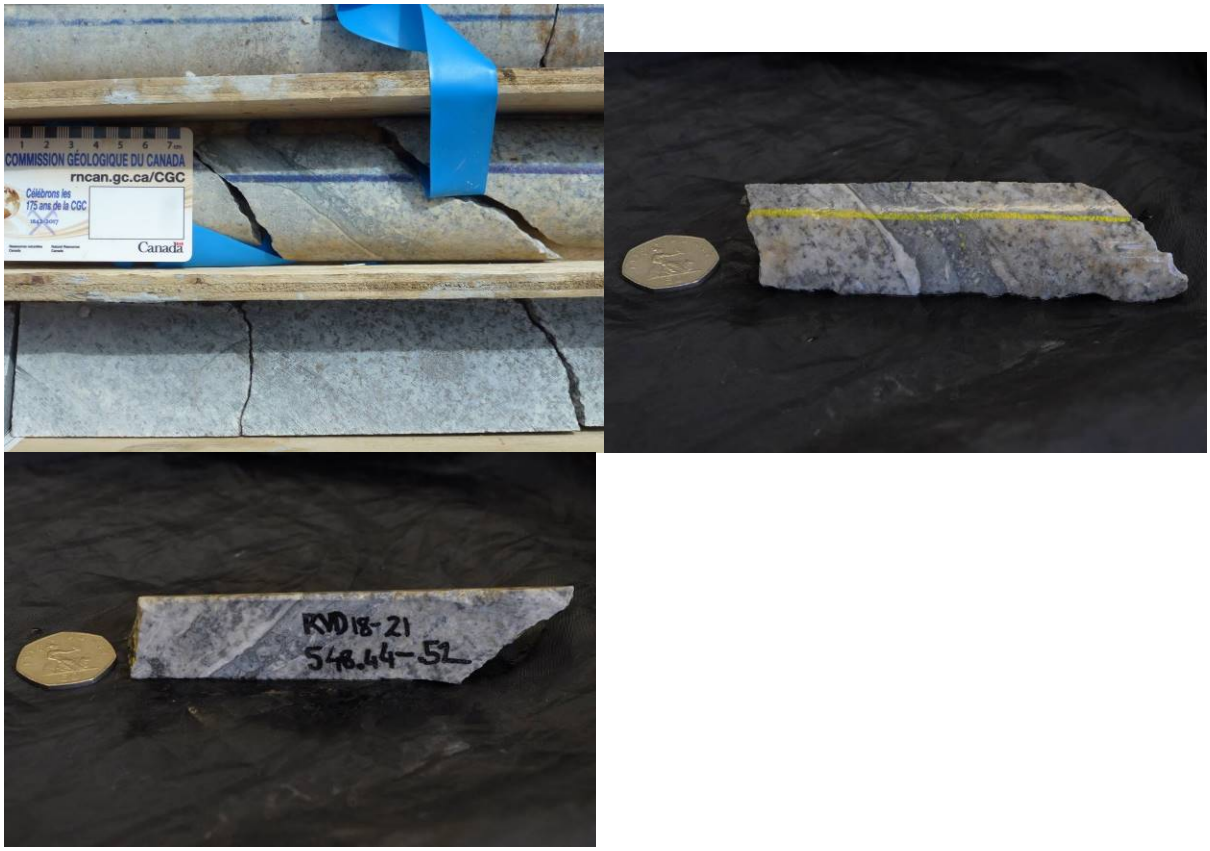

Figure 24: RVD18-21-548 core, hand specimen and thin section images

548A thin section characterization

Section 548A is comprised of several different concordant layers comprised of fine-grained silica with fragments of minerals and rock and separated by carbonate veins. The analyzed area is primarily a ~2 mm thick carbonate vein that has euhedral, elongate-blocky crystals that increase in size from the NE corner of the section (in Figure 28-30). The crystals are all pointed in the same direction (towards the SW corner in Figure 29-30), which can be interpreted to suggest that they grew uniformly from the wall rock. There is a ~1 mm thick pyrite crust on the edge of the vein with layers of very fine-grained carbonate (analyzed; Figure 30).

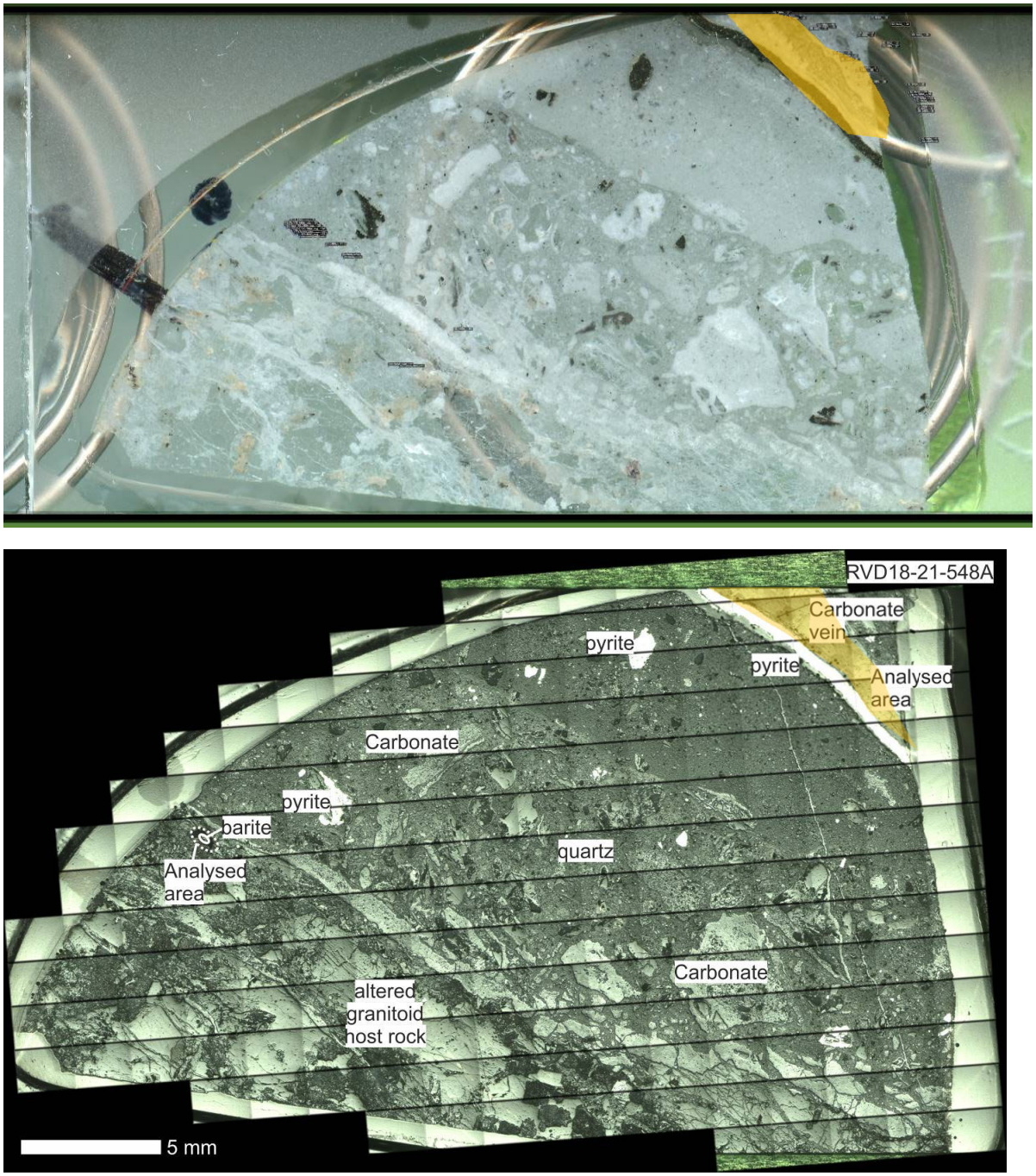

Figure 25: Section RVD18-21-548A scan and reflected light montage (as scanned image is slightly incorrectly aligned with respect to the analyzed spots). Analyzed portion of carbonate vein is highlighted in yellow.

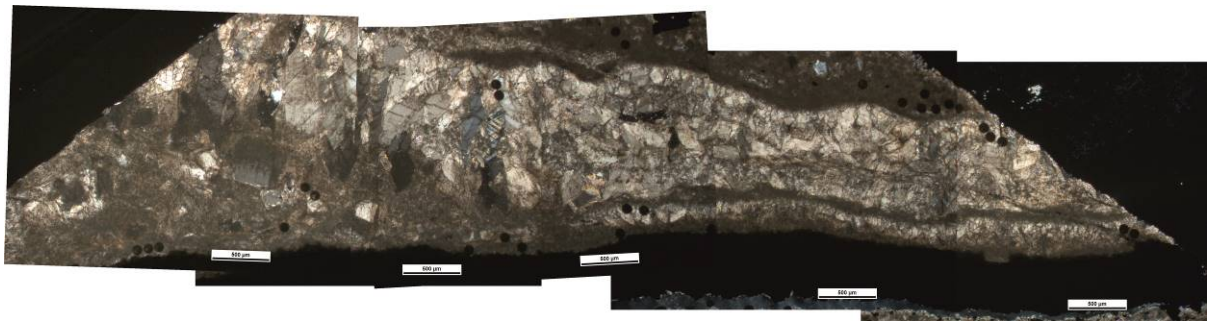

Figure 29: XPL stitched photomicrographs of vein in sample RVD19-21-548A

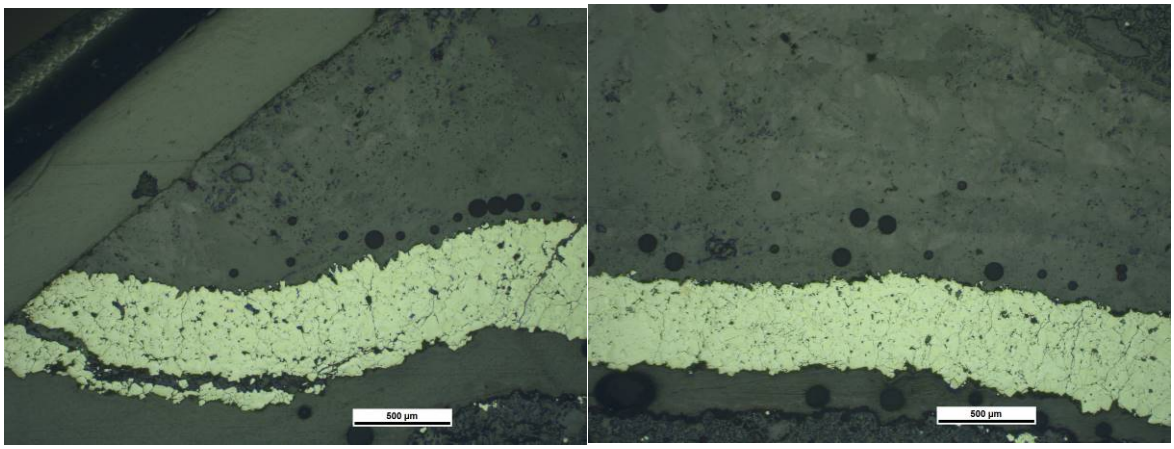

Figure 30 Reflected light image of RVD19-21-548A

548B thin section characterization

Section 548B contains the same pyrite-crusted carbonate vein described in section 548A. The section contains altered granitoid, the analyzed carbonate vein, a concordant fine-grained silica 'breccia', small fine-grained layers that can be interpreted as fault zones. The analyzed carbonate vein has euhedral blocky crystals that increase in size to ~1-2 mm in the centre of the vein (Figure 31-32). There is a pyrite crust on one edge (Figures 33-34) which can be interepreted as growth of carbonate and (re) crystallizing the pyrite at the same time.

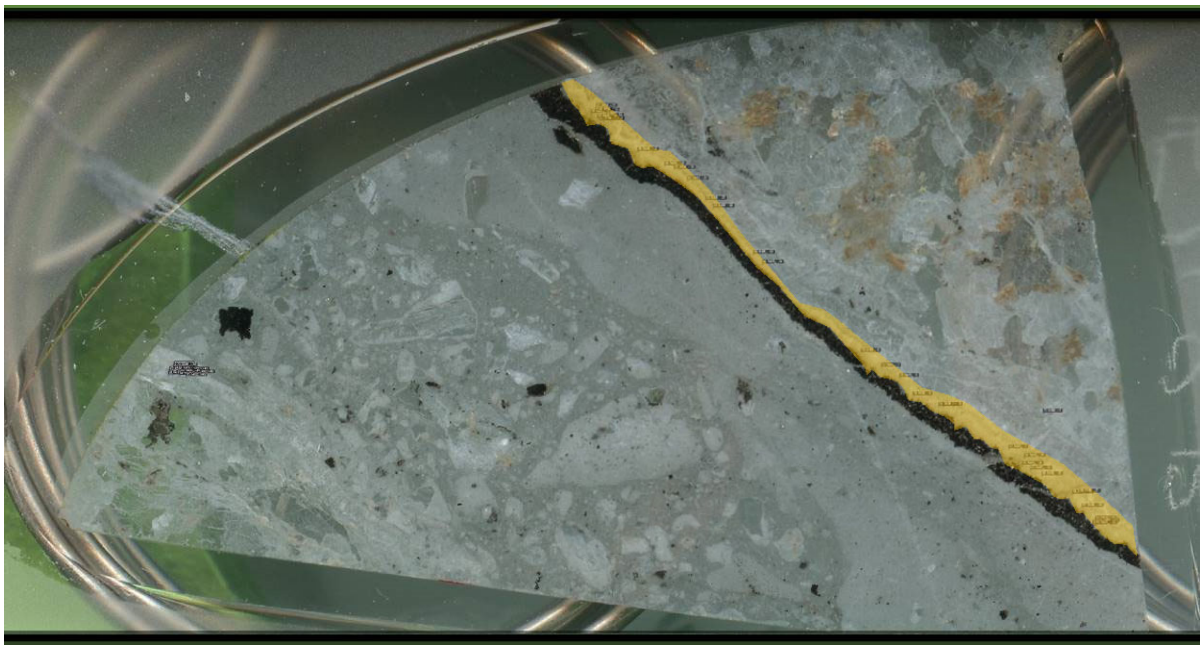

Figure 31: Section RVD18-21-548B Analyzed portion of carbonate vein is highlighted in yellow.

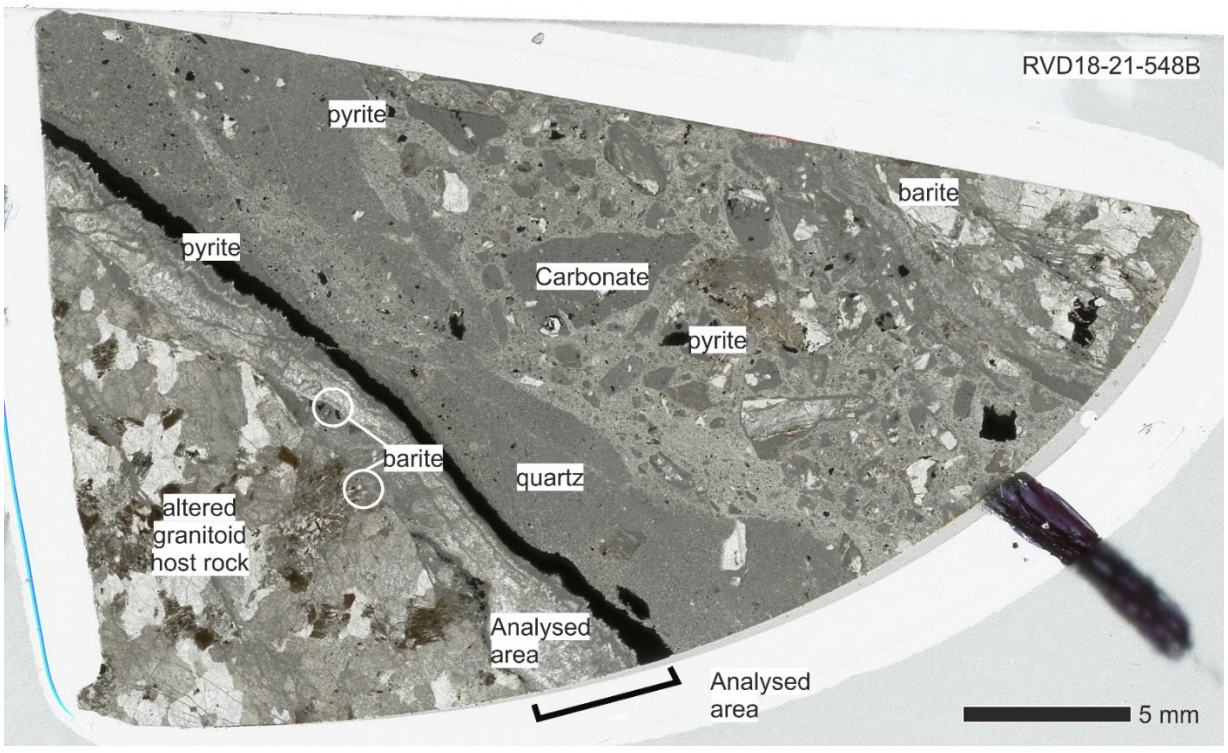

Figure 32: RVD18-21-548B with key minerals annotated

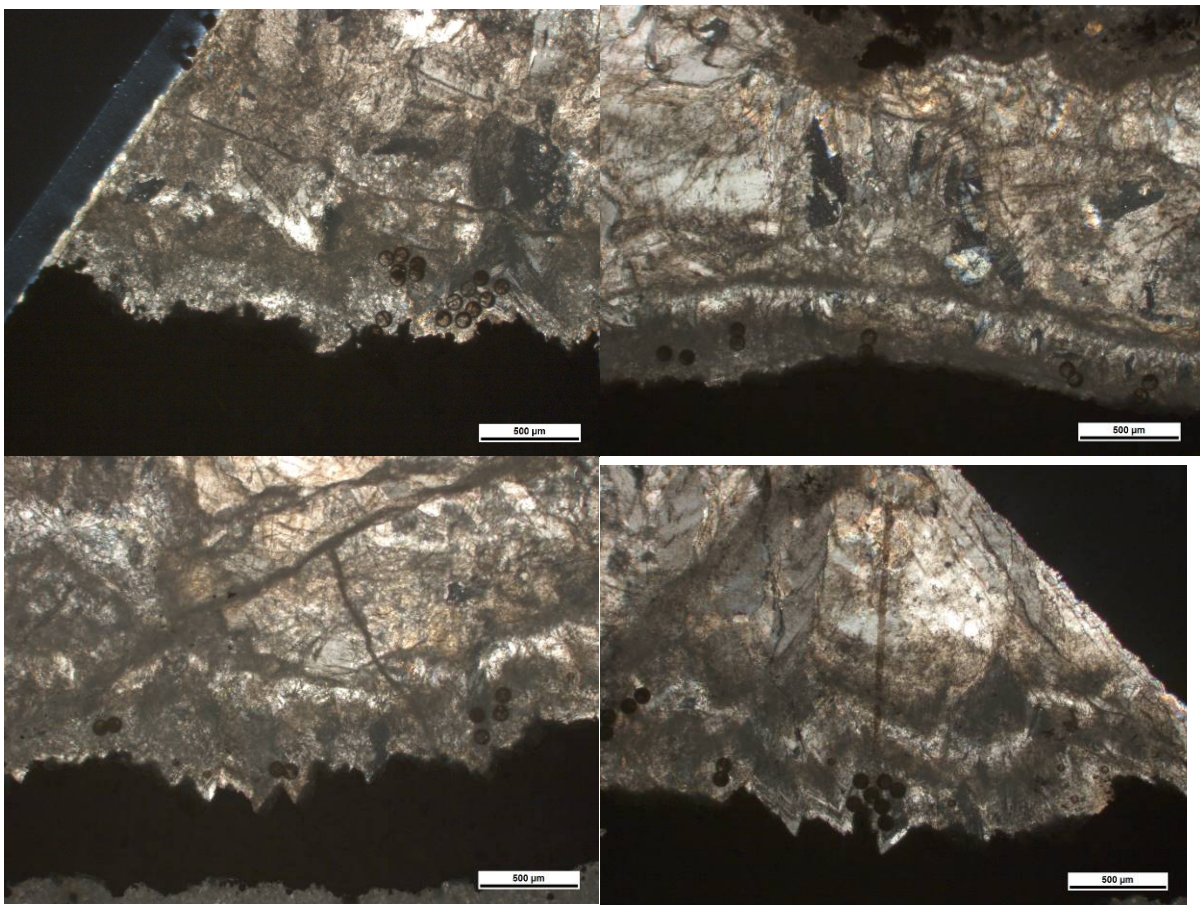

Figure 33: XPL photomicrograph of part of vein in sample RVD18-21-548B

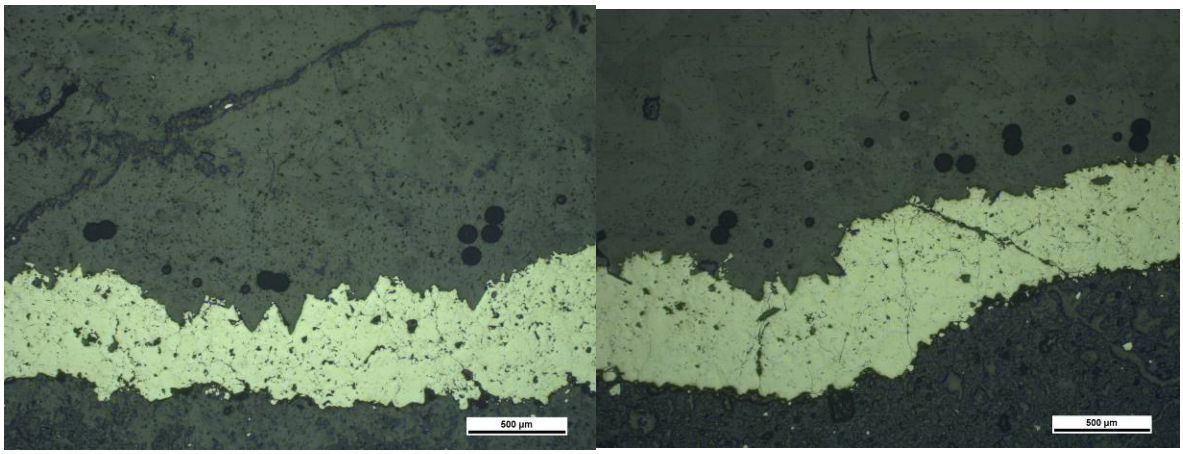

Figure 34: Reflected light image of pyrite-carbonate vein in sample RVD18-21-548B

4. Detailed U-Pb results

DDH RVD18-19, 314m (19A) detailed sample interpretation

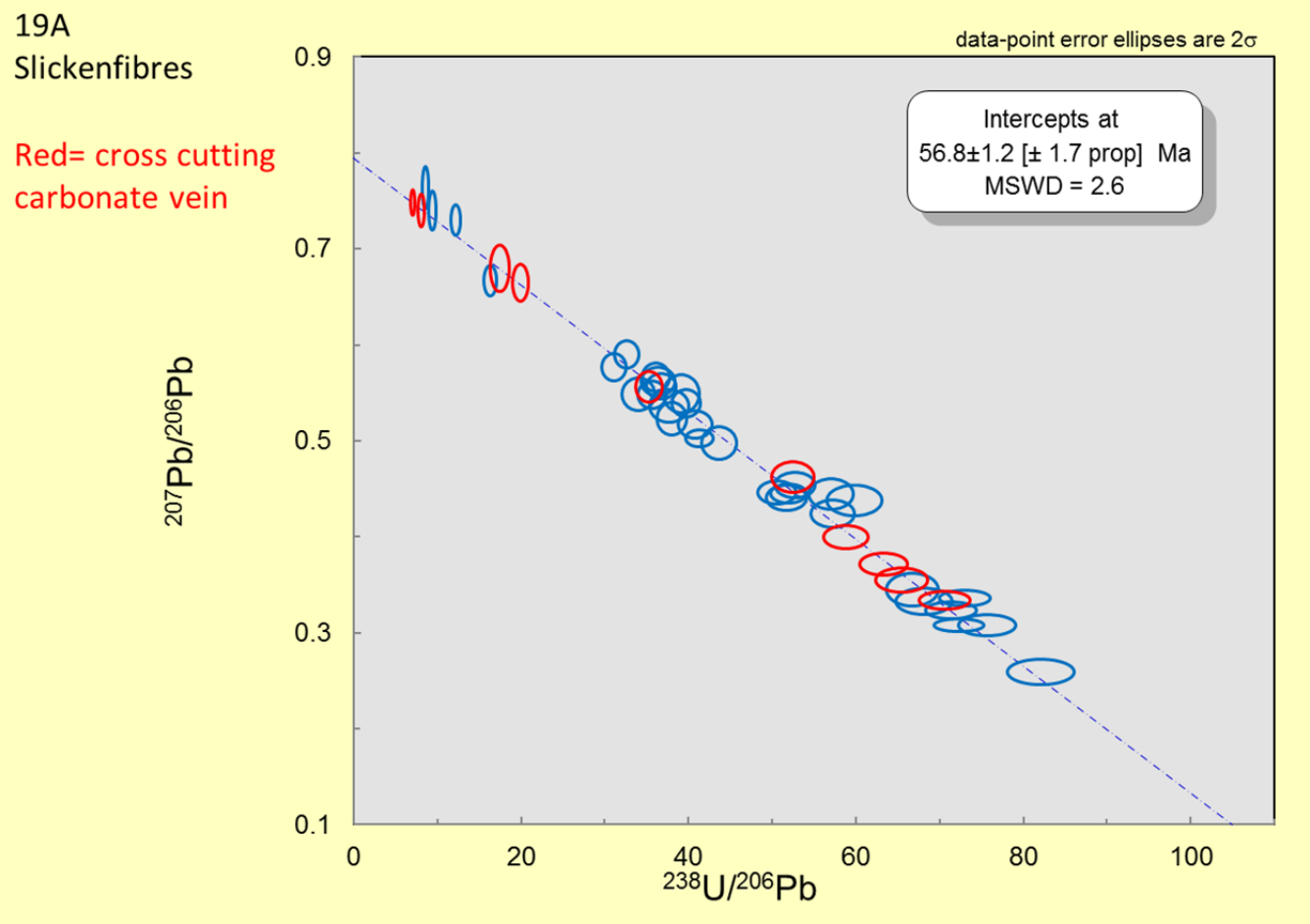

Figure 35: Tera Wasserburg plot of sample DDH RVD18-19, 314m (19A). Quoted uncertainties include fully propagated uncertainties.

The age of the sample (Fig. 35) can be interpreted as the timing of fracturing and slickenfibre growth at that time and is clearly post-dates and cross cuts the QFP dyke. As the dyke is also crosscut by mineralized veins this suggesting that the thin stringer veins and V3 veins are also post-QFP dyke emplacement. These dykes have been dated ~75 Ma (Allan et al., 2013; Friend et al., 2017) suggesting that these cross-cutting mineralized veins were emplaced between 75 and 57 Ma.

DDH RVD18-21, 542m detailed sample interpretation

- The whitish elongate-blocky crustiform carbonate with pyrite crust yields a ~73 Ma in sections A and B. The pyrite has two possible interpretations- (1) the pyrite vein is older than the carbonate and the 73 Ma carbonate vein split this older vein. (2) the pyrite is in equilibrium with the carbonate and grew as a crustiform edge on the carbonate vein. This interpretation is supported by the carbonate-pyrite crystal morphology.
- Vuggy carbonate and secondary carbonate veins crystallized at ~60 Ma.

- The multiple crack-seal events occurred in the same orientation and are also associated with polymetallic mineralization including barite. The consistency of the orientations suggests that if the veins are structurally controlled, the stress field remained roughly consistent or in a preferential orientation to reactivate these extensional fractures.

The Bluesky porphryry breccia contains abundant fault, fractures and veins. The carbonate veins dated in sample RVD-18-21-542m and 548m are roughly the same age as slickenfibres in sample DDH RVD18-19, 314m and fault gouge in sample RVD-18-21-553m, suggesting that the Bluesky porphyry breccia was fractured and faulted at the same time as fluid flow events.

DDH RVD18-21, 548 m

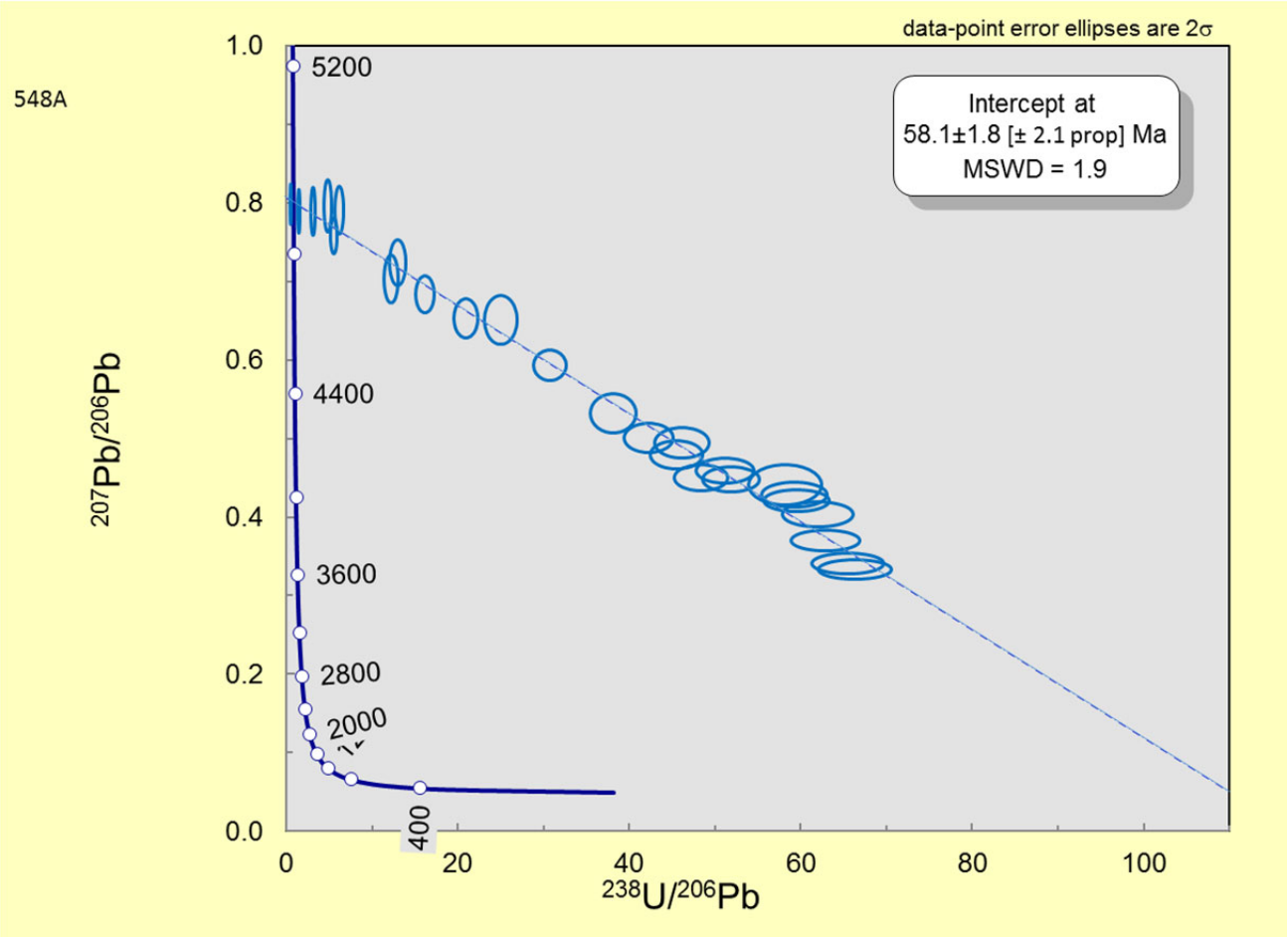

Figure 36: Tera Wasserburg plot for sample RVD-18-21-548A

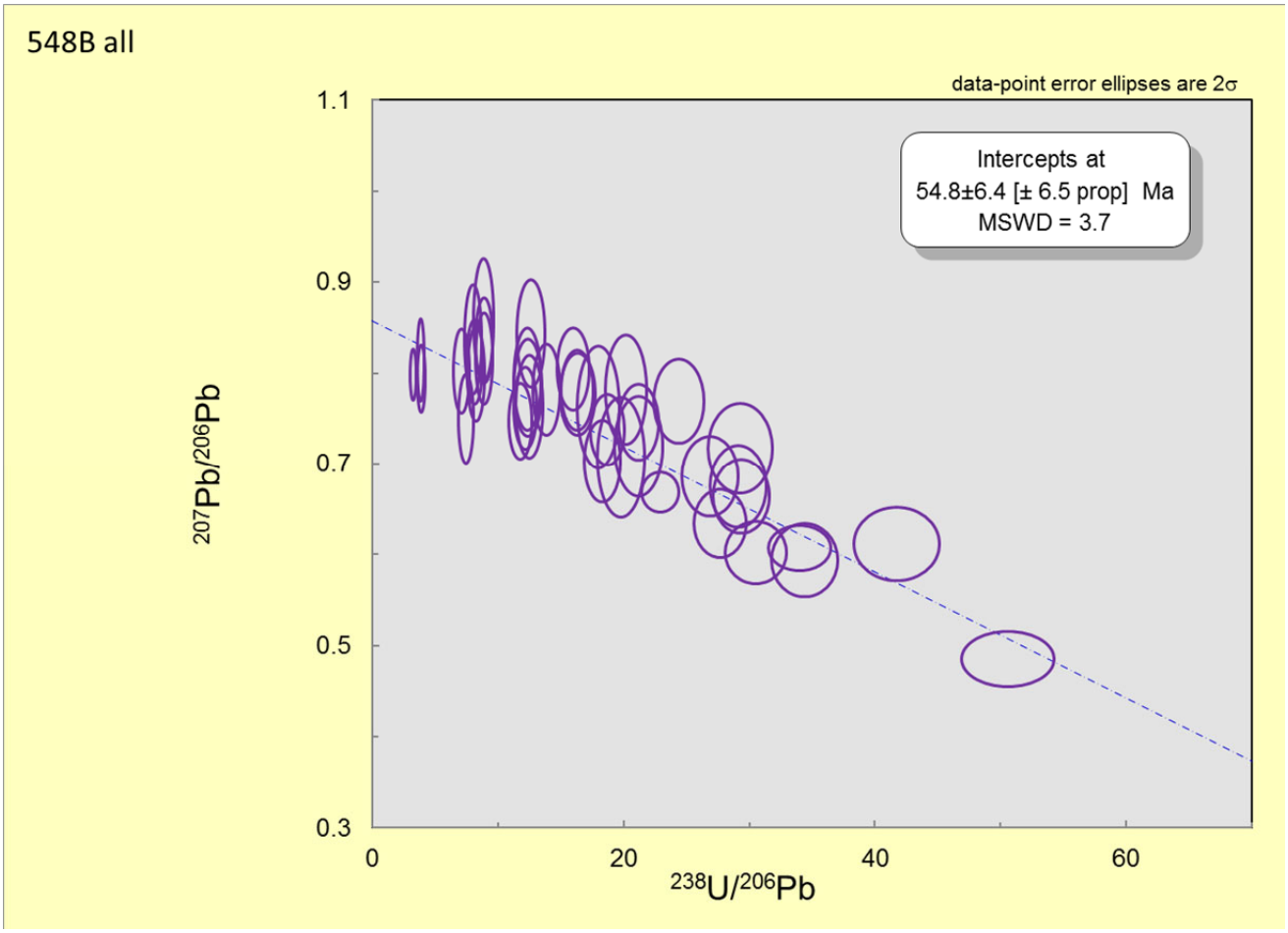

Figure 37: Tera Wasserburg plot for sample RVD-18-21-548B

Sample RVD-18-21-548A yielded ~0.05–6 ppm U and a 206Pb/238U intercept age of 58.1 ± 1.8 (MSWD 1.9; n=44). Sample RVD-18-21-548B yielded ~0.08–1.3 ppm U and a 206Pb/238U intercept of 54.8 ± 6.4 Ma (MSWD 3.7, n=29).

Interpretation

The two analysed carbonate veins from sample 548 yield inaccurate ages between ~60-55 Ma, consistent with the interpreted vuggy carbonate crystallization in sample 542 from the same core.

5. Structural data (used in Fig.1 d-e)

5.1 Planar data

Waypoint	Strike (RHR)	Dip	Description	Type
3 Big Creek road	200	87	Crush breccia	Field data
2 Big Creek road	182	52	Fault plane	Field data
2 Big Creek road	178	56	Fault plane	Field data
2 Big Creek road	183	63	Fault plane	Field data
2 Big Creek road	213	69	Fault plane	Field data

2 Big Creek road	348	70	Fault plane	Field data
2 Big Creek road	205	75	Fault plane	Field data
2 Big Creek road	255	80	Fault plane	Field data
2 Big Creek road	86	86	Fault plane	Field data
2 Big Creek road	262	86	Fault plane	Field data
2 Big Creek road	169	89	Fault plane	Field data
3 Big Creek road	193	72	Fault plane	Field data
3 Big Creek road	205	85	Fault plane	Field data
3 Big Creek road	201	85	Fault plane	Field data
3 Big Creek road	192	86	Fault plane	Field data
3 Big Creek road	200	87	Fault plane	Field data
9 Big Creek road	219	43	Fault plane	Field data
9 Big Creek road	182	82	Fault plane	Field data
10 Big Creek road	144	87	Fault plane	Field data
2 Big Creek road	187	75	fault gouge edge plane	Field data
2 Big Creek road	178	56	fault gouge edge plane	Field data
3 Big Creek road	203	70	Fault plane	Field data
3 Big Creek road	205	90	Fault plane	Field data
Seymour Creek	97	75	Gouge zone	Field data
Mechanic Creek	150	90	Gouge zone	Field data
Happy Creek	263	76	Gouge zone	Field data
Blue Sky 1	109	74	Fault within Bluesky Porphyry Breccia	Core data
Blue Sky 1	110	74	Fault within Bluesky Porphyry Breccia	Core data
Blue Sky 1	115	76	Fault within Bluesky Porphyry Breccia	Core data
Blue Sky 1	115	76	Fault within Bluesky Porphyry Breccia	Core data
Blue Sky 1	105	76	Fault within Bluesky Porphyry Breccia	Core data
Blue Sky 2	113	76	Fault within Bluesky Porphyry Breccia	Core data
Blue Sky 2	136	68	Fault within Bluesky Porphyry Breccia	Core data
Blue Sky 3	130	76	Fault within Bluesky Porphyry Breccia	Core data
Blue Sky 3	137	67	Fault within Bluesky Porphyry Breccia	Core data
Blue Sky 3	131	68	Fault within Bluesky Porphyry Breccia	Core data
Blue Sky 3	131	68	Fault within Bluesky Porphyry Breccia	Core data
Blue Sky 3	128	65	Fault within Bluesky Porphyry Breccia	Core data
Blue Sky 3	118	64	Fault within Bluesky Porphyry Breccia	Core data
Blue Sky 3	86	61	Fault within Bluesky Porphyry Breccia	Core data
Blue Sky 3	151	72	Fault within Bluesky Porphyry Breccia	Core data
Blue Sky 3	168	73	Fault within Bluesky Porphyry Breccia	Core data
Blue Sky 4	155	73	Fault within Bluesky Porphyry Breccia	Core data
RVD-18-21-542.44	239	73	Analyzed carbonate vein	Core data
RVD-18-21-548.44	242	65	Analyzed carbonate vein	Core data

5.2 Linear data

Waypoint	Trend	Plunge	Sense of movement	Description	Type
2 Big Creek road	351	15		Lineation	Field data
3 Big Creek road	120	0	?	slickenside	Field data
3 Big Creek road	249	1		Slickenside	Field data
3 Big Creek road	294	6		Slickenside	Field data
3 Big Creek road	268	5		Slickenside	Field data
4 Big Creek road	137	8	Sinistral	slickenfibre	Field data
4 Big Creek road	322	10	Sinistral	slickenfibre	Field data
4 Big Creek road	150	16		Slickenside	Field data
4 Big Creek road	126	12		Slickenside	Field data
4 Big Creek road	104	5		Slickenside	Field data
4 Big Creek road	123	10		Slickenside	Field data
4 Big Creek road	296	11		Slickenside	Field data
4 Big Creek road	295	10		Slickenside	Field data
5 Big Creek road	254	18	sinistal	slickenfibre	Field data
5 Big Creek road	255	2	sinistral	slickenfibre	Field data
5 Big Creek road	344	6	Dextral	slickenfibre	Field data
5 Big Creek road	153	10	sinistral	slickenfibre	Field data
5 Big Creek road	94	2	sinistral	slickenfibre	Field data
5 Big Creek road	86	4	sinistral	slickenfibre	Field data
5 Big Creek road	92	2	Dextral	slickenfibre	Field data
5 Big Creek road	106	48	Dextral	Slickenside	Field data
5 Big Creek road	263	48		Slickenside	Field data
5 Big Creek road	216	49	Normal	Slickenside	Field data
5 Big Creek road	86	1	Dextral	Slickenside	Field data
5 Big Creek road	246	2		Slickenside	Field data
5 Big Creek road	106	1	Sinistral	Slickenside	Field data
5 Big Creek road	261	4	Sinistral	Slickenside	Field data
5 Big Creek road	172	6	Sinistral	Slickenside	Field data
5 Big Creek road	150	8	Sinistral	Slickenside	Field data
5 Big Creek road	46	22	Sinistral	Slickenside	Field data
5 Big Creek road	16	9	Dextral	Slickenside	Field data
5 Big Creek road	248	7	Sinistral	Slickenside	Field data
5 Big Creek road	205	9	Sinistral	Slickenside	Field data
5 Big Creek road	235	24	Calcite Slickenfibre sinistral	Slickenside	Field data
5 Big Creek road	273	23	Sinistral Sample Y18-5a	Slickenside	Field data
5 Big Creek road	133	6	Sinistral	Slickenside	Field data

6 Big Creek road	347	11	Sinistral	Lineation	Field data
6 Big Creek road	332	11	Sinistral	Lineation	Field data
6 Big Creek road	148	16		Slickenside	Field data
6 Big Creek road	165	26		Slickenside	Field data
6 Big Creek road	155	7	Sinistral	Slickenside	Field data
6 Big Creek road	344	1	Sinistral	Slickenside	Field data
6 Big Creek road	306	26		Slickenside	Field data
6 Big Creek road	113	8		Slickenside	Field data
7 Big Creek road	337	22	sinistral	slickenfibre	Field data
7 Big Creek road	13	10		Slickenside	Field data
7 Big Creek road	115	17		Slickenside	Field data
7 Big Creek road	107	10		Slickenside	Field data
7 Big Creek road	110	18		Slickenside	Field data
7 Big Creek road	22	4		Slickenside	Field data
7 Big Creek road	337	22		Slickenside	Field data
8 Big Creek road	343	1	Dextral	Slickenside	Field data
8 Big Creek road	169	14	Sinistral	Slickenside	Field data
8 Big Creek road	347	9	Dextral	Slickenside	Field data
8 Big Creek road	351	20		Slickenside	Field data
10 Big Creek road	244	5	Dextral	Slickenside	Field data
10 Big Creek road	225	2	Dextral	Slickenside	Field data
10 Big Creek road	336	7	Sinistral	Slickenside	Field data
10 Big Creek road	51	17		Slickenside	Field data
10 Big Creek road	247	6	Sinistral	Slickenside	Field data
10 Big Creek road	66	1	Sinistral	Slickenside	Field data
10 Big Creek road	280	2	Sinistral	Slickenside	Field data

Brief structural interpretation

The main Big Creek Fault strands are oriented WNW-ESE with a dextral sense of shear. Slilckensides and slickenfibres measured here have both sinistral and dextral sense of shear. The BCF system likely has Riedel systems with NW-SE striking Riedel planes. The sinistal shear sense is likely yielded from conjugates of the Riedel shears (R' planes) planes.

References

Allan, M.M., Mortensen, J.K., Hart, C.J.R., Bailey, L.A., Sánchez, M.G., Ciolkiewicz, W., McKenzie, G.G., and Creaser, R.A., 2013, Magmatic and metallogenic framework of west-central Yukon and eastern Alaska. Society of Economic Geologists, Special Publication 17, p.111-168.

Black, L.P., Gulson, B.L., 1978. The age of the Mud Tank carbonatite, Strangways Range, Northern Territory. BMR J. Aust. Geol. Geophys. 3, 227 – 232.

Bonhomme, M.G., Thuizat, R., Pinault, Y., Clauer, N., Wendling, R. and Winkler, R., 1975. Méthode de datation potassium-argon. Appareillage et technique. Strasbourg, 53 p.

Dalrymple, G.B. and Lanphere, M.A., 1969. Potassium-argon dating. W.H. Freeman, San Francisco, 258 p.

Dickin, A.P., 1995. Radiogenic isotope geology. Cambridge University Press, Cambridge, 490 p.

Faure, G., 1986. Principles of isotope geology. John Wiley & Sons, New York, 589 p.

Friend, M.A., Allan, M.M., and Hart, C.J.R., 2017, New contributions to the bedrock geology of the Mount Freegold district, Dawson Range, Yukon (NTS 115I/2, 6 and 7). *In*: MacFarlane, K.E. (ed.) Yukon Exploration and Geology 2017. Yukon Geological Survey, p.47-68.

Heinrichs, H. and Herrmann, A.G., 1990. Praktikum der Analytischen Geochemie. Springer-Verlag, Berlin-Heidelberg, 669 p.

Hess, J.C. and Lippolt, H.J., 1994. Compilation of K-Ar measurements on HD-B1 standard biotite. in: Odin G.S. (1994): Phanerozoic time scale, Bull. Lias. Inform., IUGS subcom. Geochronol., 12, Paris p. 19-23.

Jackson, S. E., Pearson, N. J., Griffin, W. L., & Belousova, E. A. (2004). The application of laser ablation-inductively coupled plasma-mass spectrometry to in situ U–Pb zircon geochronology. *Chemical Geology*, *211*(1-2), 47-69.

Ludwig, K. R. (2003). Isoplot 3.00: A geochronological toolkit for Microsoft Excel. *Berkeley Geochronology Center Special Publication*, *4*, 70.

McDougall, I. and Roksandic, Z., 1974. Total fusion 40Ar/39Ar ages using HIFAR reactor. Journal of the Geological Society of Australia 21, 81-89.

Odin, G.S. & 35 collaborators 1982. Interlaboratory standards for dating purposes. in: ODIN, G.S. (editor) Numerical Dating in Stratigraphy. Part 1. John Wiley & Sons, Chichester, 123-148.

Parrish, R. R., Parrish, C. M., & Lasalle, S. (2018). Vein calcite dating reveals Pyrenean orogen as cause of Paleogene deformation in southern England. *Journal of the Geological Society*, *175*(3), 425-442.

Paton, C., Hellstrom, J., Paul, B., Woodhead, J., & Hergt, J. (2011). Iolite: Freeware for the visualisation and processing of mass spectrometric data. *Journal of Analytical Atomic Spectrometry*, *26*(12), 2508-2518.

Pearce, N. J., Perkins, W. T., Westgate, J. A., Gorton, M. P., Jackson, S. E., Neal, C. R., & Chenery, S. P. (1997). A compilation of new and published major and trace element data for NIST SRM 610 and NIST SRM 612 glass reference materials. *Geostandards Newsletter*, *21*(1), 115-144.

Roberts, N. M., Rasbury, E. T., Parrish, R. R., Smith, C. J., Horstwood, M. S., & Condon, D. J. (2017). A calcite reference material for LA-ICP-MS U-Pb geochronology. *Geochemistry, Geophysics, Geosystems*, *18*(7), 2807-2814.

Stacey, J. T., & Kramers, 1. (1975). Approximation of terrestrial lead isotope evolution by a two-stage model. *Earth and planetary science letters*, *26*(2), 207-221.

Steiger, R.H. and Jäger, E. 1977. Subcommission on Geochronology: convention on the use of decay constants in geo-and cosmochronology. Earth and Planetary Science Letters 36, 359-362.